Final State Interactions in $^{3}\vec{He}(\vec{e}, e'p)$

INAUGURAL-DISSERTATION

zur
Erlangung der Würde eines Doktors der Philosophie
vorgelegt der
Philosophisch-Naturwissenschaftlichen Fakultät
der Universität Basel

von

Cédric Carasco
aus Saint-Denis (France)

Basel 2004

Genehmigt von der Philosophisch-Neturwissenschaftlichen Fakultät
auf Antrag von Professor Dr. I. Sick und PD Dr. J. Jourdan.

Basel, den 8. Juni 2004

Professor Dr. Marcel Tanner
Dekan

With distinction "magna cum laude".

Acknowledgments

I would like to thank my supervisors, Ingo Sick and Jürg Jourdan, for their support and their advises, for having given to me the great opportunity to take part in so many experiments during my thesis.

I would like to thank Ernst Wilhelm Otten and Werner Heil who welcomed me in their team.

I would like to thank all my shift and setup companions, with whom I shared so many good moments, not only during experiments but also during the many other occasions that working in a team offers.

I would like to mention:

- Jörg Bermuth, for his support, and for having introduced me in the ^{3}He world.
- Daniela Rohe, for her support and for her advises in writing this thesis.
- Glen Warren, for his help and his explanations concerning Cola++, the MAMI Spectrometer hall software.
- Markus Hauger, Kristoff Normand, Thomas Petitjean and Hartmut Wöhrle who greatly helped in building the hadron detector in the hall.
- Jörg Schmiedeskamp for his work concerning the polarization of the target.
- The MAMI staff, for its manpower support and for having made possible such an experiment.
- Peter Schmid and Hartmut Wöhrle for they efficient work in maintaining our computers and our network.

Abstract

The goal of this thesis is to investigate final state interactions in quasielastic scattering of polarized electrons on a polarized helium 3 target in order to correct measurements of the neutron electric form factor at Q^2=0.67(GeV/c)^2.
The rescattering effect was focused upon via the measurement of asymmetries in $^3\vec{H}e(\vec{e},e'p)$. The measurements were done at the microtron MAMI in Mainz. Results of data analysis show that the rescattering effect is well approximated with the spectator approximation which therefore allows the neutron electric form factor to be corrected from rescattering effects.
Finally, it is shown that one can fully correct the electric form factor from final state interactions at Q^2=0.67(GeV/c)^2.

Introduction

My thesis involves the study of rescattering reactions which affect the measurement of the electric form factor of the neutron at large momentum transfer. The electric from factor of the neutron, which describes the electric structure of the neutron, is not well known. Therefore, its measurement is of particular importance. Since, in nature, no free neutron target exists, one has to study properties of the neutron with neutrons bound in light nuclei. Polarized helium 3 targets can be considered as free neutron targets. By measuring asymmetries in quasielastic scattering of polarized electrons on polarized helium 3, one can measure the neutron electric from factor. In such a reaction, the scattered electron is detected together with the recoiling neutron. However, one has to take into account the effect of the protons in the final state of the reaction. Such effects can be fully calculated when the momentum transfered to the neutron is low. At large momentum transfer, where we want to do the measurement, it is not possible to fully calculate these final state interactions. Approximations are however still possible and can be tested by measuring asymmetries when the scattered electron is detected together with the recoiling proton.

Contents

1 Neutron electric form factor 1

1.1 Nucleon form factors 1

1.2 Polarized ^3He : a polarized neutron target 4

1.2.1 Spin structure of ^3He 4

1.2.2 Formalism for $^3\vec{H}e(\vec{e},e'p)$ 5

1.3 Beyond PWIA 6

1.3.1 Final Sate Interactions in $^3He(e,e'n)$ 6

1.4 Faddeev formalism 7

1.4.1 Handling relativity 11

2 Experiment 15

2.1 Setup 15

2.1.1 Detectors 15

2.1.2 Coincidence logic 18

2.2 Polarized electron beam 19

2.3 Polarized ^3He target 20

2.3.1 Presentation 20

2.3.2 Magnetic field optimization 23

3 Analysis 27

3.1 Proton detection 27

3.1.1 Introduction 27

3.1.2 Proton definition 28

3.1.3 Position measurement 33

3.2 Polarization product measurement 34

4 Results and conclusion 37

4.1 Results 37

4.2 Discussion 40

4.3 Conclusion 41

A Magnetic field optimization 43

B Edge effect 47

B.1 Qualitative understanding 47

B.2 Quantitative understanding 49

C Pile up and position measurement 55

D Optimal combination of measurements 59

List of Figures

1.1 G_e^n measured with different methods. 3

1.2 Spin structure of ^3He 4

1.3 Kinematics of $^3He(e,e'n)$ 5

1.4 3 nucleons interacting via pairwise potentials 8

1.5 Expansion of FSI in a scattering series. One circle represents one scattering between the corresponding nucleons. 10

1.6 The two aspects of FSI in $^3He(e,e'n)$ 11

1.7 Spectator approximation. 12

2.1 Experimental setup 16

2.2 Detection system of spectrometer A 17

2.3 The hadron detector 18

2.4 Logic driving hadron detector-spectrometer coincidences 19

2.5 Three step processes involved in the production of polarized electrons. 20

2.6 Metastable optical pumping of ^3He 21

2.7 Quartz cell containing the polarized ^3He 22

2.8 Target box with coils defining the field direction. Only one turn per coil is drawn. 24

2.9 Coils current divider 25

2.10 Shape of the free induction decay at different spin angles 26

3.1 ΔE-paddle spectrum with the proton cut 27

3.2 E_p versus ω. The calculation use equation (3.3) 29

3.3 Positions of the copper wires used in the energy loss calculations . 30

3.4 Examples of selected events in the hadron detector 31

3.5 T_e after the Cherenkov and proton cuts 31

3.6 Electron equivalent energy loss spectrum versus ω for two bars from the last layer of the hadron detector. 32

3.7 Scattered electron energy spectra together with asymmetries. . . . 35

4.1 Energy transfer spectrum with the two selected regions 38

4.2 Asymmetries integrated over region 2. The results of the full(PWIA) calculations are shown in blue full(dashed). The result of a full calculation using a non-relativistic current with relativistic kinematics (green dot) and with non-relativistic kinematics (green dot-dashed) are also shown. 39

4.3 Same as figure 4.2 but for an integration over region 1. 39

A.1 Positions where one could measure the field to do the correction properly 45

B.1 ADC ratio versus TDC difference of PMs from the same bar . . . 47

B.2 Light propagation in the scintillator 48

B.3 Edge effect in the light collection 49

B.4 Scintillator with the definition of the axis. 50

B.5 Algorithm describing the path of the light inside the scintillator. . 51

B.6 Path lengh distribution of a ray that reaches S+, without light attenuation (red) and with light attenuation (black). 52

B.7 Comparison of the measured ADCs ratio shape with simulations. . 53

B.8 Probabilities to lose a ray (red curves) and to detect a ray (green curves) versus the position of the proton in the bar, with U=0.5. . 53

C.1 σ_X versus $\widetilde{r}$, with E=300 ADC channels, D=50cm and $\lambda = 320cm$. 57

C.2 Error distribution for different values of $\widetilde{r}$ 57

List of Tables

3.1 Materials and thicknesses crossed by the proton 30
3.2 Polarization product measurements for the 4 target spin angles. . 36

D.1 Error associated with the different covariance matrices 63

Chapter 1

Neutron electric form factor

1.1 Nucleon form factors

A large part of our knowledge concerning the structure of nucleons and nuclei is based on electron scattering experiments. The electron-nucleon interaction is well understood in Quantum Electro Dynamics (QED) and can be handled perturbatively. This allows for a clear separation of the reaction mechanism and the nuclear structure.

Since the 30^{ties}, we know that protons and neutrons are not pointlike particles [1, 2, 3]. Being composite systems, they have an internal structure. Two phenomenological quantities are needed to describe the scattering of electrons from a nucleon : the electromagnetic Sachs form factors G_e and G_m [4]. They provide the information about charge and magnetization distributions of the nucleons.

The two form factors appear explicitly in the scattering cross section (1.1) (known as the Rosenbluth cross section [5]) for electron-nucleon scattering from a nucleon N in the one photon exchange approximation.

$$\frac{d\sigma}{d\Omega}(Q^2) = \left(\frac{d\sigma}{d\Omega}\right)_{Mott}(Q^2)\left[\frac{G_e^{N^2}(Q^2)+\tau G_m^{N^2}(Q^2)}{1+\tau}+2\tau G_m^{N^2}(Q^2)\tan^2\left(\frac{\theta_e}{2}\right)\right]. \tag{1.1}$$

In (1.1), $\tau = \frac{Q^2}{4M}$ and θ_e is the scattering angle of the electron. M is the nucleon mass and Q^2 the four momentum transferred to the nucleon. $\left(\frac{d\sigma}{d\Omega}\right)_{Mott}$ describes the cross section for electron scattering from a pointlike spinless nucleon.

In the Breit frame, where no energy is transferred to the nucleon N, G_e^N is the Fourrier transform of its charge density and G_m^N is the Fourrier transform of its magnetization density [4].

In the first approach to access these form factors, the ratio $R = \left(\frac{\partial\sigma}{\partial\Omega}\right) / \left(\frac{\partial\sigma}{\partial\Omega}\right)_{Mott}$ was measured for a constant Q^2 at different θ_e. One determines G_e^N and G_m^N from the slope and intercept of $R(\tan^2(\theta_e))$. This technique, known as the Rosenbluth separation, was successfully used for measuring G_e^p and G_m^p [6, 7].

As there are no free neutron targets in nature, electron scattering from neutrons bound in light nuclei must be used. The disadvantage is obvious since nuclear structure effects have to be incorporated in the description of the scattering process. In addition, further effects like Final State Interactios (FSI) and Meson Exchange Currents (MEC) complicate the interpretation of the measurements.

For the determination of G_m^n , one overcomes such complications using the cross section ratio of $D(e,e'n)$ and $D(e,e'p)$. In such a ratio, nuclear structure effects cancel and FSI and MEC effects are small, which allows for a reliable determination of G_m^n , with an accuracy better than 2% [8].

Platchkov et al., in [9], extract G_e^n from the deuteron $A(Q^2)$ structure function measured in elastic electron-deuteron scattering. However, such determinations have large uncertainties due to model dependence of the nucleon-nucleon interaction. These uncerntainties can be seen in fig. 1.1, which shows various measurements of G_e^n , where the $A(Q^2)$ lines are spline fits made from G_e^n determinations done with different potentials. The use of the deuteron quadrupole form factor $F_Q(Q^2)$ reduces the model dependence and leads to more accurate estimates of G_e^n [10].

Polarization observables involve interference terms which contain the electromagnetic form factors. Thus, polarization observables are good candiates for an accurate determination of G_e^n [11]. G_e^n can be extracted from polarization observables in $\vec{D}(\vec{e},e'n)p$, $D(\vec{e},e'\vec{n})p$, and also in ${}^3\vec{H}e(\vec{e},e'n)X$ [12], where X stands for a deuteron or a unbound np system.

Using polarized ${}^3He$, G_e^n has been measured at Q^2=0.37(GeV/c)^2 [13] and at Q^2=0.67(GeV/c)^2 [14]. Today's measurements of G_e^n are shown in fig. 1.1. The Gastler parametrization [15] is also shown in fig. 1.1. It can be written as $G_e^n = \frac{a_G\tau}{1+b_G\tau}\cdot\frac{1}{1+Q^2/\Lambda_D^2}$, with $a_G = 1.91$, $b_G = 5.6$ and $\Lambda_D = 0.71$.

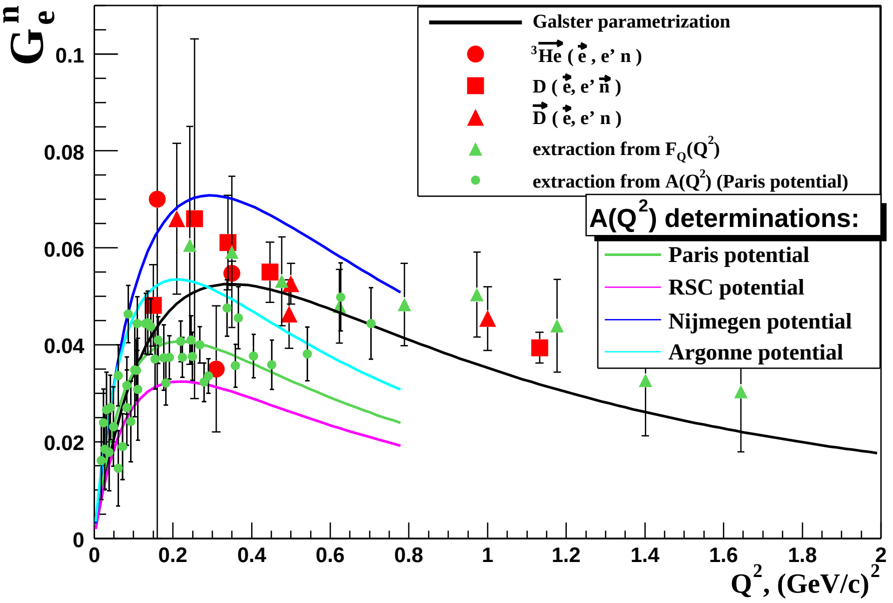

Figure 1.1: G_e^n measured with different methods.

1.2 Polarized ^3He : a polarized neutron target

1.2.1 Spin structure of ^3He

^3He is made of two protons and one neutron. One expects that the two protons couple together and cancel their spin contribution to the total nuclear spin J. In such a picture, the ^3He spin is carried only by the unpaired neutron.

Since J=$\frac{1}{2}$=L+S, with L the orbital angular momentum of ^3He, partial waves with $L \neq 0$ contribute to the ^3He wave function [16].

Calculations of the ^3He ground state using a realistic nucleon-nucleon interaction potential predict that about 90% of the ^3He wave function is in a symmetric S state (L=0,S=$\frac{1}{2}$, see fig. 1.2). In such a state, the 2 protons couple to spin 0: the neutron alone carries the nuclear spin [17, 18], as it is naively expected. Thus, to about 90%, a polarized ^3He target can be seen as a polarized neutron target [19]. This makes ^3He particularly attractive for neutron studies via polarization observables.

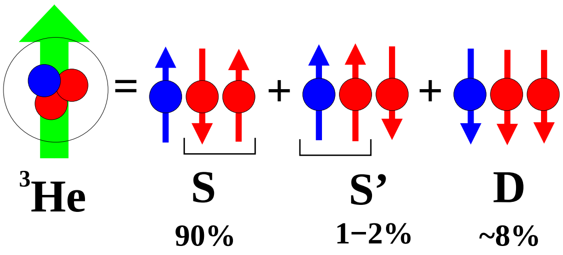

Figure 1.2: Spin structure of ^3He

1.2.2 Formalism for $^3\vec{H}e(\vec{e},e'p)$

G_e^n can be extracted from asymmetries being measured in exclusive quasielastic $^3\vec{H}e(\vec{e},e'p)X$ scattering with longitudinally polarized electrons and polarized ^3He target.

The incident electron, with a 4-momentum $(E,\overrightarrow{k})$ and a defined spin state $s=\pm\frac{1}{2}$, corresponding to the helicity $h=\pm 1$, is scattered into a 4-momentum $(E',\overrightarrow{k'})$. The energy and momentum transferred to the neutron bound in ^3He are respectively $\omega = E - E'$ and $\overrightarrow{q} = \overrightarrow{k} - \overrightarrow{k'}$, which defines the 4-momentum transfer $Q^2 = \omega^2 - |\overrightarrow{q}|^2$.

Relative to the scattering plane defined by $(\overrightarrow{k},\overrightarrow{q})$ (see fig. 1.3) the $\overrightarrow{^3He}$ spin is defined by an in-plane polar angle θ^* and an out of plane azymuthal angle ϕ^*.

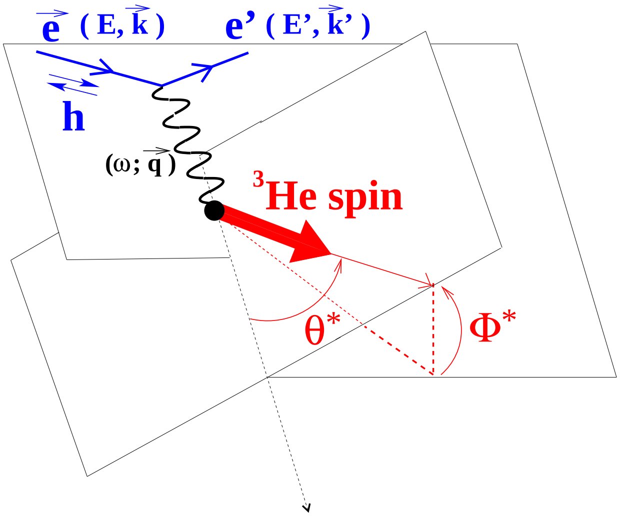

Figure 1.3: Kinematics of $^3He(e,e'n)$

In the one photon exchange approximation, the cross section can be written as:

$$\frac{d\sigma}{d\Omega}(\theta^*,\phi^*) = \Sigma\,(\theta^*,\phi^*) + h\cdot\Delta\,(\theta^*,\phi^*)\,. \tag{1.2}$$

Depending on the $^3\vec{H}e$ spin direction, one can extract G_e^n from asymmetries

$$A(\theta^*,\phi^*) = \frac{\Delta\,(\theta^*,\phi^*)}{\Sigma\,(\theta^*,\phi^*)} = \frac{aG_e^nG_m^n\sin(\theta^*)\cos(\phi^*) + bG_m^{n\ 2}\cos(\theta^*)}{G_e^{n\ 2} + cG_m^{n2}}, \tag{1.3}$$

where $a = 2\sqrt{\tau(\tau+1)}\tan(\theta_e/2)$, $b = 2\tau\sqrt{1+\tau+(1+\tau)^2\tan^2(\theta_e/2)}\tan(\theta_e/2)$ and $c = \tau + 2\tau(1+\tau)\tan^2(\theta_e/2)$. If one defines $A_z = A(0°, 0°)$ and and $A_x = A(90°, 0°)$ and ignores interactions between the nucleons (plane wave impulse approximation, PWIA), 1.3 yields

$$G_e^n(Q^2) = K \cdot G_m^n(Q^2) \cdot \left(\frac{A_x}{A_z}\right)(Q^2), \tag{1.4}$$

with $K = \sqrt{\tau + \tau(1+\tau)\tan^2(\frac{\theta_e}{2})}$.

For nucleon momenta below 100MeV/c, it has been shown in [20] that a polarized ^3He target can be seen as a polarized neutron target. Thus, ignoring FSI and MEC (1.4) can be used to extract G_e^n from the measured asymmetries.

1.3 Beyond PWIA

Two nuclear medium effects must be considered : Final State Interactions (FSI) and Meson exchange Currents (MEC). MEC are due to the fact that inside a nucleus nucleons interact very strongly via meson exchange. Because of such interactions, electrons can interact with the exchanged meson. In a Feynman diagram, this can be seen as the absorption of the virtual photon by a π or ρ meson exchanged between the two interacting nucleons [21]. However, working at the top of the elastic peak as we did, theoretical calculations show that MEC effects are small. FSI, on the other hand, cannot be neglected when scattering electrons on nuclei [22].

1.3.1 Final Sate Interactions in $^3He(e, e'n)$

Just after the electron is scattered, the three nucleons are still very close and they mutually interact via the strong force, modifying so the final asymptotic state seen by the detectors.

Thus, the full description of FSI is a problem of describing the interactions between three nucleons after absorption of the virtual photon by one of them. Since the 90^{ties}, it is possible in a quantitative approach to solve the three-body wave function not only for the ground state but also for continuum state which implicitly accounts for all possible FSI effects [23].

1.4 Faddeev formalism

At low and medium energy, below the pion threshold, the interaction between two nucleons is described with a realistic non-relativistic nucleon-nucleon potential. The wave function $|\Psi_{3N}\rangle$ which describes a system of 3 nucleons (labeled 1,2,3) interacting via pairwise nucleon-nucleon potentials is given by the non-relativistic Schrödinger equation

$$(H_0 + V_{12} + V_{23} + V_{13})\Psi_{3N} = E\Psi_{3N}, \tag{1.5}$$

where V_{ij} is the interaction potential between nucleons i and j (fig. 1.4) and H_0 is the Hamiltonian which describes the dynamics of three free nucleons[1]. The amplitude for the virtual photon absorption takes the from

$$\langle\Psi_{final}|\mathbf{j}|\Psi_{^3He}\rangle, \tag{1.6}$$

where $\mathbf{j}$ is the single nucleon current operator, $|\Psi_{^3He}\rangle$ represents the initial hadronic state (^3He bound state) and $\langle\Psi_{final}|$ is the final hadronic state subsequent to the absorption of the photon by one of the nucleons. To take FSI into account, one has to use the wave function $|\Psi_{3N}\rangle$ representing three interacting nucleons [23] as a final state in (1.6). Introducing the three nucleons propagator $G_0 = (E - H_0)^{-1}$,

---

[1] The 2-body breakup of the initial ^3He system must also be included in the description of the reaction. Then, instead of a free 3-body hamiltonian, one has to use a Hamiltonian describing the dynamics of a free nucleon-nucleon bound state together with a free nucleon state.

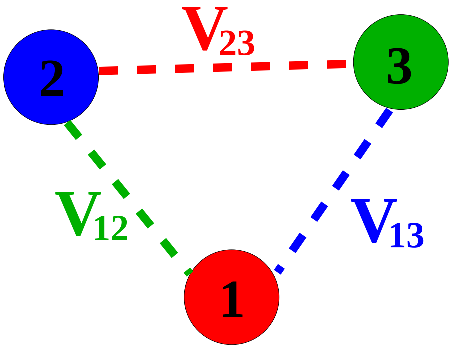

Figure 1.4: 3 nucleons interacting via pairwise potentials

(1.5) can be written in the form

$$\Psi_{3N} = \Phi_0 + G_0(V_{12} + V_{23} + V_{13})\Psi_{3N}. \tag{1.7}$$

The inhomogeneous term Φ_0 (which, under PWIA, is the final state in (1.6)) describes a system of three non interacting nucleons, and being so, is a solution of the free Schrödinger equation

$$H_0\Phi_0 = E\Phi_0. \tag{1.8}$$

Writing $\Psi_{ij} = G_0 V_{ij}\Psi_{3N}$, Ψ can be seen as the sum of three wave functions, the Faddeev components:

$$\Psi = \Psi_{12} + \Psi_{13} + \Psi_{23}. \tag{1.9}$$

Applying V_{ij} in (1.7) and reordering the equations, the initial Schrödinger equation (1.7) becomes equivalent to a system of three coupled equations,

$$\Psi_{12} = \Phi_{12} + G_0 T_{12}(\Psi_{23} + \Psi_{13}), \tag{1.10}$$

$$\Psi_{23} = \Phi_{23} + G_0 T_{23}(\Psi_{13} + \Psi_{12}), \tag{1.11}$$

$$\Psi_{13} = \Phi_{13} + G_0 T_{13}(\Psi_{12} + \Psi_{23}), \tag{1.12}$$

where T_{ij} is the 2-body T matrix, which gives the scattering dynamics between nucleons i and j. Φ_{ij} is the wave function describing a system where nucleons i and j scatter, the third nucleon being free. Such a wave function is solution of the inhomogeneous equation

$$\Phi_{ij} = \Phi_0 + G_0 T_{ij} \Phi_0. \tag{1.13}$$

The situation can be simplified noticing that protons and neutrons are identical particles, provided one labels them with the appropriate isospin quantum numbers. Considering three identical particles, one can use permutation operators P_{ij} which exchange positions of particle i and j. All Faddeev components can then be written as a function of only one of them. Finally, one ends with only one integral equation

$$\Psi = \Phi + G_0 T P \Psi, \tag{1.14}$$

where $P = P_{13}P_{23} + P_{12}P_{23}$ and the inhomogeneous term Φ is a solution of

$$\Phi = \Phi_0 + G_0 T \Phi_0. \tag{1.15}$$

The full wave function Ψ_{3N} is finally given by

$$\Psi_{3N} = (1 + P)\Psi. \tag{1.16}$$

Description of FSI

After iteration of (1.14) and (1.15), (1.6) becomes:

$$\begin{aligned} \langle \mathbf{\Phi_0} | (\mathbf{1} + \mathbf{P})\mathbf{j} | \mathbf{\Psi_{^3He}} \rangle + \langle \Phi_0 | \mathrm{TG_0(1+P)j} | \Psi_{^3\mathrm{He}} \rangle \\ + \langle \Psi | P T G_0 (1+P) j | \Psi_{^3He} \rangle \end{aligned} . \tag{1.17}$$

The first matrix element, $\langle \Phi_0 | (1+P) j | \Psi_{^3He} \rangle$, allows the photon to be absorbed by one of the three nucleons, since $(1+P)j = \sum_{i=1}^{3} j_i$, i being the nucleon label. Iterating again (1.14) and (1.15) in (1.17), one gets

$$\begin{aligned} \langle \mathbf{\Phi_0} | (\mathbf{1} + \mathbf{P}) \mathbf{T} \mathbf{G_0} (\mathbf{1} + \mathbf{P}) \mathbf{j} | \mathbf{\Psi_{^3He}} \rangle + \langle \Phi_0 | \mathrm{TG_0PTG_0(1+P)j} | \Psi_{^3\mathrm{He}} \rangle \\ + \langle \Psi | P T G_0 T G_0 (1+P) j | \Psi_{^3He} \rangle . \end{aligned} \tag{1.18}$$

The matrix element $\langle\Phi_0|(1+P)TG_0(1+P)j|\Psi_{^3He}\rangle$ is the next order of the expansion. After the absorption of the photon $((1+P)j)$, the three nucleons propagate (G_0), scatter two by two $((1+P)T)$ and end in a free state (Φ_0). The next iteration gives

$$\begin{aligned}\langle\boldsymbol{\Phi_0}|(\mathbf{1}+\mathbf{P})\mathbf{TG_0PTG_0}(\mathbf{1}+\mathbf{P})\mathbf{j}|\boldsymbol{\Psi}_{^3\mathbf{He}}\rangle + \langle\Phi_0|\mathrm{TG_0PTG_0TG_0}(1+\mathrm{P})\mathrm{j}|\Psi_{^3\mathrm{He}}\rangle \\ +\langle\Psi|TG_0PTG_0PTG_0TG_0(1+P)j|\Psi_{^3He}\rangle\end{aligned}. \tag{1.19}$$

$\langle\Phi_0|(1+P)TG_0PTG_0(1+P)j|\Psi_{^3He}\rangle$ describes all possible scatterings between two different pairs of nucleons, after a free propagation between each scattering. The next iteration describes all scatterings between three different pairs of nucleons, and so on.

The expansion of the matrix element (1.6) leads to a multi scattering series with increasing number of scatterings between the nucleons, a free propagation being introduced between each scattering. This series is represented in fig. 1.5.

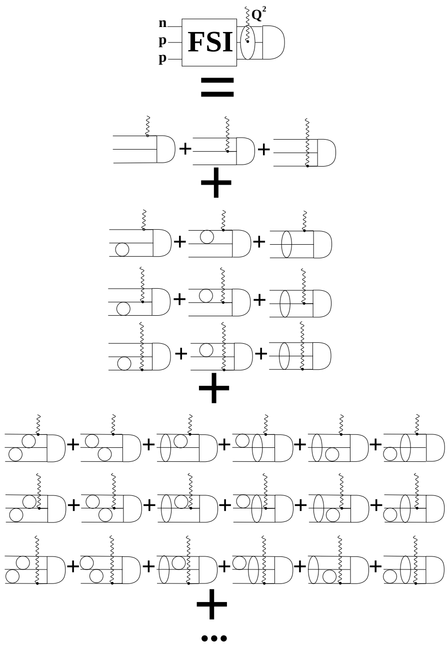

Figure 1.5: Expansion of FSI in a scattering series. One circle represents one scattering between the corresponding nucleons.

One can distinguish between two aspects of FSI shown in fig. 1.6. In the first one, the neutron absorbs the photon and is detected after some scattering with the protons. This is the rescattering process. In the second case, the photon is absorbed by one of the protons. After scatterings between all nucleons, the neutron is accidentally scattered away, seen by the detectors and misunderstood as a neutron which firstly interacted with the electron. This is the charge exchange process.

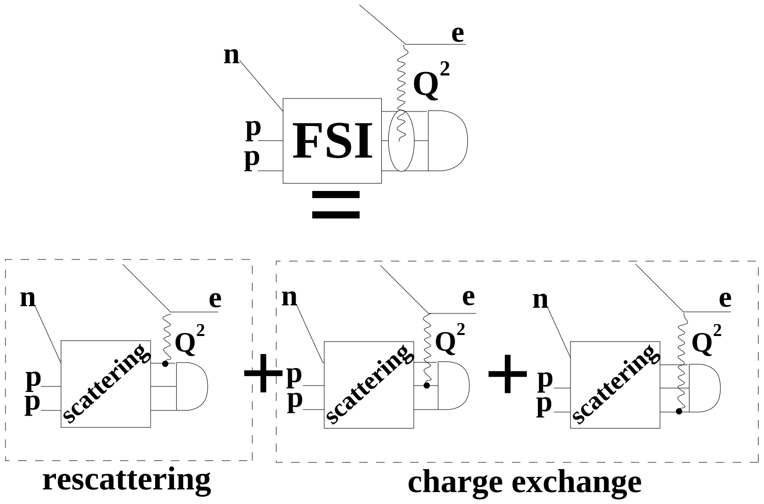

Figure 1.6: The two aspects of FSI in $^3He(e,e'n)$

1.4.1 Handling relativity

The full calculation of the series is reliable only below the pion threshold, at low and medium energy transfers [24]. At high momentum transfer, a full calculation is not consistent in particular because of the use of the non-relativistic phenomenologic nucleon-nucleon potentials in (1.5). Thus, an alternative approach has been suggested for the calculation of the FSI correction. In this approach, one keeps only the low energy spectator interaction in the FSI calculations, but relativity is included in the kinematics and the currents.

One must then answers two questions:

- Can one reliably approximate FSI at high momentum transfer using the spectator approximation shown in fig. 1.7?
- Is there a way to experimentally assess the amplitude of the charge exchange process and its effect on the measurement of G_e^n?

One has to find relevant observables to answer these two questions.

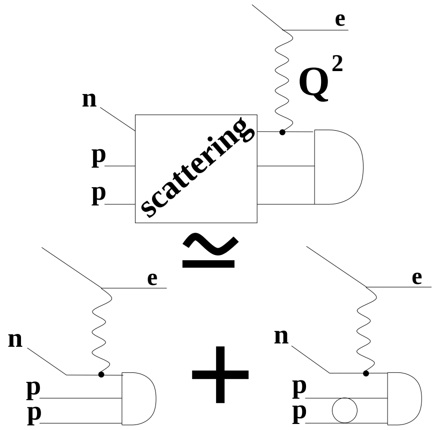

Figure 1.7: Spectator approximation.

Charge exchange process

Investigation of charge exchange is done via the $^3\vec{He}(e,e'n)$ reaction. One scatters unpolarized electrons on polarized ^3He . The ^3He spin can be switched between $\phi^* = 90^o$ or $\phi^* = -90^o$, perpendicular to the reaction plane. One measures the asymmetry A_y^0 between $\frac{d\sigma}{d\Omega}(\phi^* = 90^o)$ and $\frac{d\sigma}{d\Omega}(\phi^* = -90^o)$. Calculations and experiment made at low Q^2 show that A_y^0, which is zero under PWIA [25], is a good observable for measuring the amplitude of charge exchange process [26].

Details concerning this measurement are given in the PhD thesis of Merle [27] (in German).

Rescattering process

The validity of the spectator approximation shown in fig. 1.7 is checked with asymmetry measurements in $^3\vec{H}e(\overrightarrow{e}, e'p)$. Since A_z and A_x are very small in the $^3\vec{H}e(\overrightarrow{e}, e'p)$ reaction, they are observables sensitive to FSI. They represent interesting observables for our investigation. The measurement of A_z and A_x for the $^3\vec{H}e(\overrightarrow{e}, e'p)$ reaction is described in the remainder of this thesis.

Chapter 2

Experiment

2.1 Setup

2.1.1 Detectors

The ${}^3\vec{H}e(\vec{e},e'p)$ experiment took place at the Mainz electron facility MAMI, simultaneously with the ${}^3\vec{H}e(\vec{e},e'n)$ experiment which aimed at a measurement of G_e^n at $Q^2 = 0.67(\mathrm{GeV/c})^2$ [28]. The microtron delivered a 10μA continuous wave beam of 855MeV polarized electrons [29]. Electrons were scattered on a 4 bar polarized ${}^3He$ gas target provided by the Physical Institut of the Mainz University [28].

The detection setup is shown in fig. 2.1. Spectrometer A detects the scattered electrons coming from the ${}^3\vec{H}e(\vec{e},e'n)$ reaction or from the ${}^3\vec{H}e(\vec{e},e'p)$ reaction. Elastically scattered electrons from ${}^3\vec{H}e(\vec{e},e')^3He$ are detected by spectrometer B in order to measure the beam-target polarization product (see section 3.2). Protons and neutrons are detected by Basel's hadron detector shown in fig. 2.3.

Spectrometer A [30] is a Quadrupole-Sextupole-Dipole-Dipole magnet system which covers a solid angle of 28msr and has a momentum acceptance of $\Delta p/p$=20%.

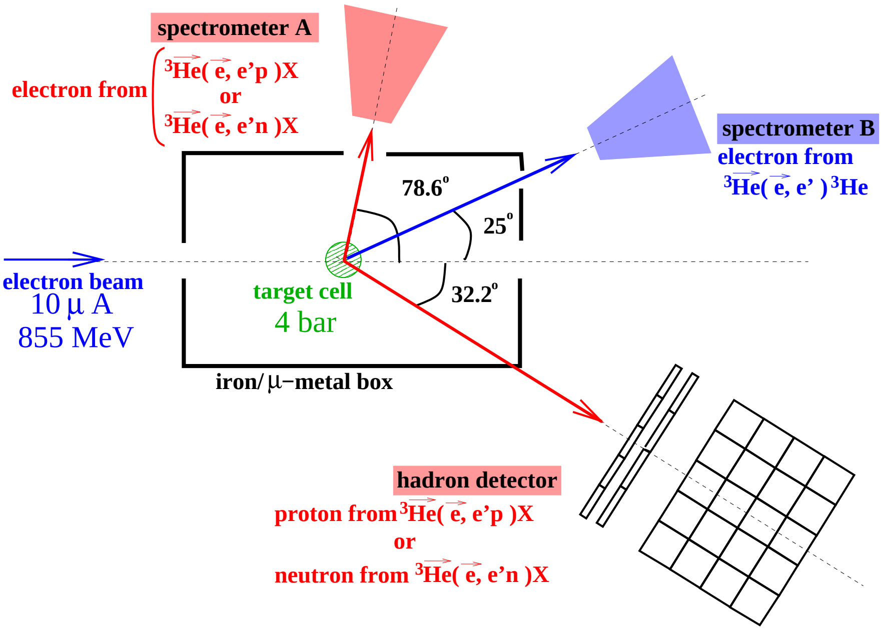
spectrometer A
electron from
$^3\vec{\mathrm{He}}(\vec{e}, e'p)X$
or
$^3\vec{\mathrm{He}}(\vec{e}, e'n)X$
spectrometer B
electron from
$^3\vec{\mathrm{He}}(\vec{e}, e')^3\mathrm{He}$
78.6°
25°
32.2°
electron beam
10 μ A
855 MeV
target cell
4 bar
iron/μ–metal box
hadron detector
proton from $^3\vec{\mathrm{He}}(\vec{e}, e'p)X$
or
neutron from $^3\vec{\mathrm{He}}(\vec{e}, e'n)X$

Figure 2.1: Experimental setup

Its central momentum is set to 492.9(MeV/c) for this experiment. Focal plane coordinates are measured by vertical drift chambers (the VDCs in fig. 2.2).

Two segmented planes of plastic scintillators (ΔE_1 and ΔE_2 in fig. 2.2) provide the trigger which starts the VDC drift-time measurement. These scintillators also provide the trigger used to make the coincidence between the spectrometer and the hadron detector.

Spectrometer A is equipped with a Cherenkov threshold detector which allows to discriminate electrons from heavier charged particles.

Spectrometer B consists of a single dipole magnet, covering 5.6msr, and a momentum acceptance of 15%. It is equipped with a similar set of detectors as spectrometer A.

The hadron detector's central part is made of 20 vertical BC400 scintillator bars (E-bars, blue in fig. 2.3). Each E-bar (50cm×10cm×10cm) is connected to a photomultiplier on both sides (PM_{up} and PM_{down}, red in fig. 2.3). PMs and plastic scintillators are connected via BC800 light guides, (gray in fig. 2.3). Two layers of 2cm thick BC400 scintillators (ΔE-paddle, green in fig. 2.3) are placed in front of the E-bars. All ΔE-paddles are coupled to one PM.

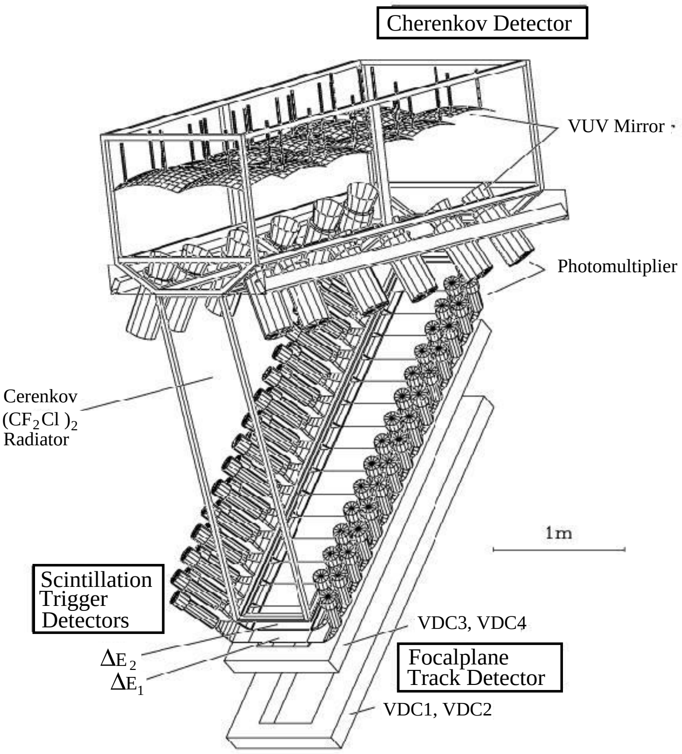
Cherenkov Detector
VUV Mirror
Photomultiplier
Cerenkov
(CF$_2$Cl)$_2$
Radiator
1m
Scintillation
Trigger
Detectors
VDC3, VDC4
ΔE_2
ΔE_1
Focalplane
Track Detector
VDC1, VDC2

Figure 2.2: Detection system of spectrometer A

If the quantity of light seen in one of the E-bars is bigger than a given threshold, the hadron detector triggers. The nature of the particle (proton or neutron) seen by the hadron detector depends on the signal of the ΔE-paddles. Protons always produce a clear signal when crossing a ΔE-paddle, whereas neutrons rarely interact in such thin plastic layers. Therefore, with its ΔE-paddle, the hadron detector can discriminate neutrons (measurement of G_e^n) from protons (present investigation of FSI).

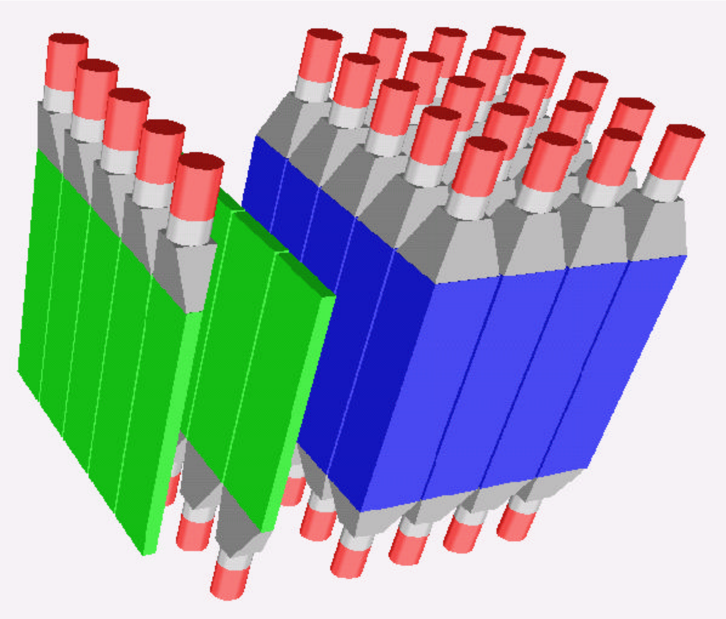

Figure 2.3: The hadron detector

2.1.2 Coincidence logic

The logic circuit used for this experiment is sketched in fig. 2.4. When spectrometer A and the hadron detector trigger at the same time, all PMs are read out. Their output current is integrated and digitized by Analog to Digital Converters (ADC).

The first E-bar of the hadron detector crossing the threshold gives a starting time. A PM crossing the discrimination threshold later gives its own stopping time. The time elapsed between the common start and the individual stops is measured and digitized by a Time to Digital Converter (TDC). Therefore, for each E-bar, one gets ADC and TDC informations for PM_{up} (ADC_{up} and TDC_{up}) and for PM_{down} (ADC_{down} and TDC_{down}). Since spectrometer A provides a stopping time, also the time information T_e is recorded for electrons.

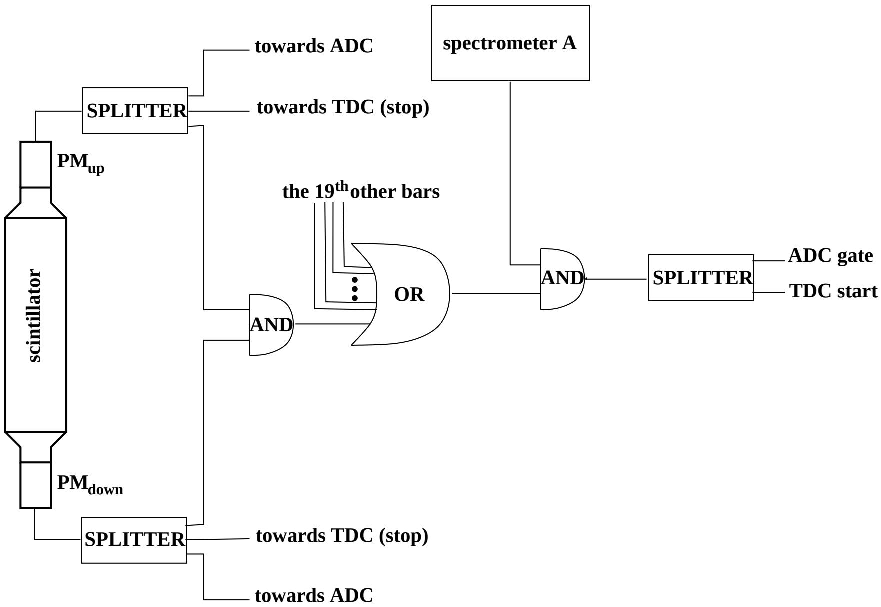
towards ADC
spectrometer A
SPLITTER
towards TDC (stop)
PM$_{up}$
the 19thother bars
scintillator
OR
AND
AND
SPLITTER
ADC gate
TDC start
PM$_{down}$
SPLITTER
towards TDC (stop)
towards ADC

Figure 2.4: Logic driving hadron detector-spectrometer coincidences

2.2 Polarized electron beam

The MAMI source of polarized electrons uses photoemission from a GaAsP semiconductor crystal [29]. The photoemission process is done in three steps sketched in fig. 2.5. Electrons which absorb the circularly polarized light propagate towards the semiconductor surface. Due to the cesium-oxygen layer covering the semiconductor, the electron affinity at the surface is negative, allowing the electrons to escape into vacuum [31]. The electrons are then guided to the microtron [32] and accelerated up to 855MeV. The beam polarization P_e, which was typically about 80%, was measured every day with a Møller polarimeter.

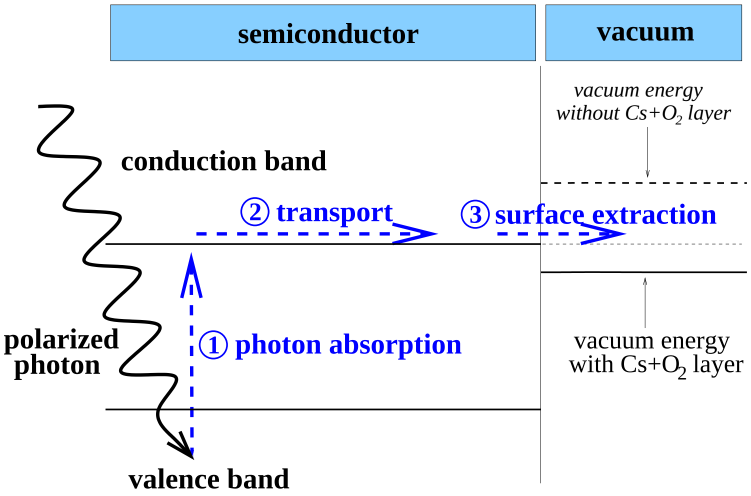
semiconductor
vacuum
vacuum energy without Cs+O$_2$ layer
conduction band
② transport
③ surface extraction
① photon absorption
polarized photon
vacuum energy with Cs+O$_2$ layer
valence band

Figure 2.5: Three step processes involved in the production of polarized electrons.

2.3 Polarized ^3He target

2.3.1 Presentation

It is known since long that ^3He can be polarized by means of optical pumping [33], but it is only since about fifteen years that technology improvements and efforts allow the production of large quantities of dense polarized ^3He [34].

The ^3He can be polarized either by the so-called spin-exchange technique which involves spin-exchange collisions between ^3He and polarized rubidium vapor [35], or by metastable optical pumping. Only metastable optical pumping will be discussed in the following.

The different processes involved in the optical pumping of ^3He are shown in fig. 2.6. Low pressure radio frequency discharges bring ^3He atoms from the 1^1S_0 ground state to the long lived 2^3S_1 metastable state. The absorption of right handed polarized photons allows the transition from the hyperfine levels $m_F = -\frac{1}{2}, m_F = -\frac{3}{2}$ to the $m_F = \frac{1}{2}, m_F = -\frac{1}{2}$ levels of the 2^3P_0 shell. Reemission

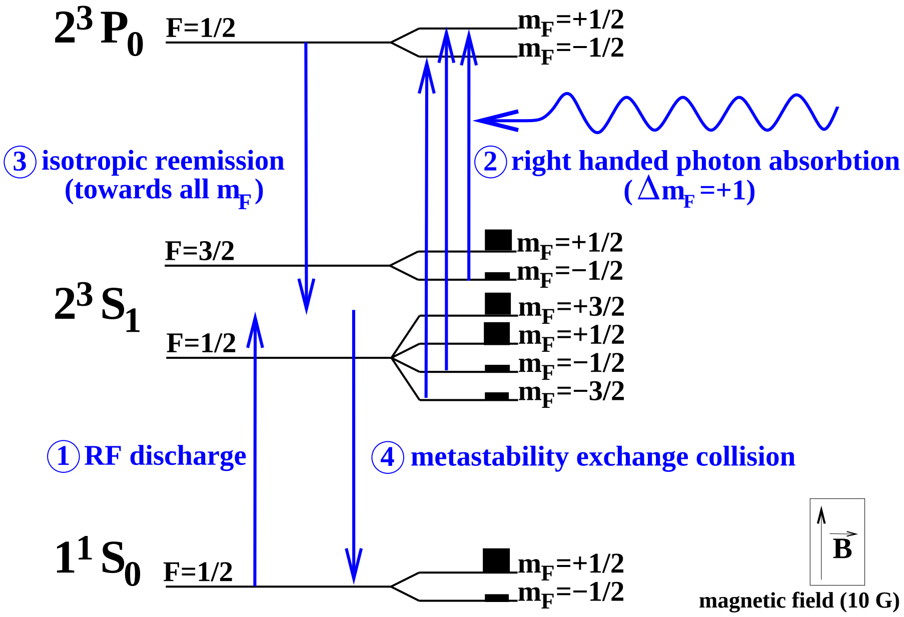
2^3P_0
F=1/2
m_F=+1/2
m_F=−1/2
③ isotropic reemission
(towards all m_F)
② right handed photon absorbtion
(Δm_F=+1)
F=3/2
2^3S_1
F=1/2
m_F=+1/2
m_F=−1/2
m_F=+3/2
m_F=+1/2
m_F=−1/2
m_F=−3/2
① RF discharge
④ metastability exchange collision
1^1S_0
F=1/2
m_F=+1/2
m_F=−1/2
$\vec{B}$
magnetic field (10 G)

Figure 2.6: Metastable optical pumping of ^3He

from the 2^3P_0 shell brings ^3He atoms back into all levels of the 2^3S_1 shell. In this way in the 2^3S_1 shell one obtains a net increase of ^3He atoms oriented in the $m_F > 0$ states. Metastability exchange collisions [36] transfer the polarization from the metastable state to the nuclear spin of the ground state. Since all these processes work only efficiently at low pressure (≈1mbar), the gas has to be compressed after the polarization process in order to reach dense polarized targets of about 4 bars. The gas is kept in cesium coated cells shown in fig. 2.7. Details concerning targets production can be found in the thesis of Bermuth [28] or Rohe [37] (both in German). After pumping, ^3He targets have an initial polarization of about 50%[1].

This polarization decreases exponentially because of various relaxation processes. The overall relaxation time T_1 is given by

$$\frac{1}{T_1} = \sum_i \frac{1}{T_i}, \tag{2.1}$$

---

[1] With the newly developed compressor and laser system, 74% polarization is currently achieved [38].

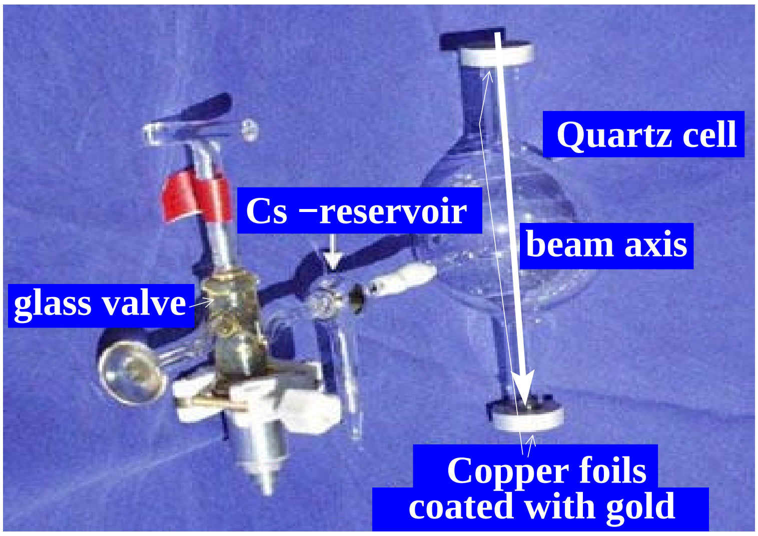

Figure 2.7: Quartz cell containing the polarized ^3He

where T_i is the characteristic time corresponding to the depolarization process i. Dipole interactions between ^3He atoms [39] contribute to the depolarization of the gas. For a gas at pressure p, the characteristic time is $T_{dipole} = \frac{817\ h \cdot bar}{p} = 204$h for a 4bar cell. Another source of depolarization comes from paramagnetic centers on the cell inner surface. Coating the inner surface with cesium brings the corresponding characteristic time to about $T_{surface} = 125$h, this value shows large variations from one cell to the other. Interactions of polarized ^3He atoms with $^3He^+$ or $^3He^{++}$ ions , produced when the beam is passing through the gas, contribute also to depolarize the gas [40, 41]. The corresponding characteristic time is about 170h. Finally, magnetic field inhomogeneities (field gradients) depolarize the target [42] with a characteristic time

$$T_{gradient} = \alpha^{-1} \left(\frac{B_0}{\frac{\partial B_0}{\partial r}} \right)^2 \cdot p, \quad \alpha = 17500 \text{ cm}^2 \text{ bar h}^{-1}. \tag{2.2}$$

With typical relative field gradients of $5{\cdot}10^{-4}$cm, after optimization of the field, one reaches $T_{gradient}$ ≈1000h for p=4bars.

During the experiment, T_1 was about 35h [28]. To keep a reasonable level of polarization, targets were changed two times a day.

One could think that the beam looses some polarization when crossing the target windows (25μm). But such losses are negligible. Indeed, following [43], the relative loss of polarization is $\frac{\Delta P}{P} = \frac{\varepsilon}{2(E+Ix_0)} \approx 1^\circ/_{\circ\circ}$, where $I \cdot x_0 = 23MeV$ is the collision energy loss times the radiation length, E is the beam energy and $\varepsilon = 0.7MeV$ is the total energy loss of the electron in the copper window.

The absolute polarization P_t of the target is measured using the Adiabatic Fast Passage technique (AFP) [44]. AFP consists in reversing the direction of the ^3He spins by means of a radio frequency excitation. Measuring the magnetic field before and after the spins change their direction, one sees a field jump equal to two times the field induced by the polarized target. With the knowledge of the cell geometry and pressure, one recovers the polarization with an accuracy of about 3% [28]. AFP measurements were done after each spin rotation ($\approx$ every 3 hours). To monitor the loss of polarization faster, some complementary Nuclear Magnetic Resonance measurements (NMR) were done every half hour. However, NMR measurements give only a relative polarization measurement. Because of the unavoidable electromagnetic noise in the experimental hall, the signal to noise ratio of the NMR measurements is quite bad, as is revealed by a simple look at fig. 2.10. Thus, the NMR is less accurate as the AFP.

2.3.2 Magnetic field optimization

To protect the gas against external magnetic fields, which come mostly from the spectrometers, the target is kept in an iron-μ-metal box shown in fig. 2.8. The spin-holding field ($\approx$ 8 Gauss) is obtained using three main coils shown in fig. 2.8.

With these holding fields alone, relative field gradients as large as $5 \cdot 10^{-3}\text{cm}^{-1}$ can be seen by the ^3He atoms, leading to $T_{gradient} \approx 10\text{h}$. To correct such inhomogeneities, each of the main coils is coupled to four smaller correction coils

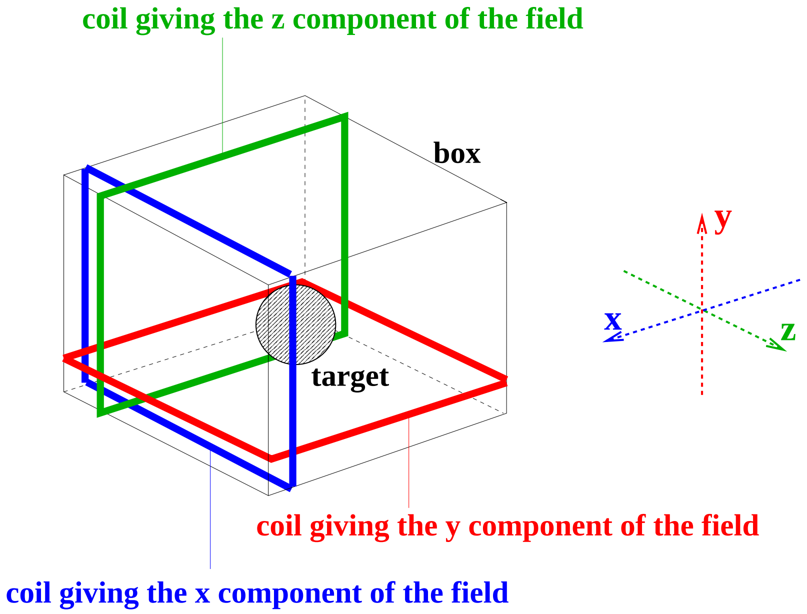
coil giving the z component of the field
box
target
y
x
z
coil giving the y component of the field
coil giving the x component of the field

Figure 2.8: Target box with coils defining the field direction. Only one turn per coil is drawn.

(current divider shown in fig. 2.9).

The field B_i produced by a correction coil is

$$B_i(x) = P_i(x) \cdot I_i, \qquad i \in \{1, 2, 3, 4\}, \tag{2.3}$$

where I_i is the current passing through the coil. Its amplitude is determined by the potentiometer resistance value. The proportionality factor $P_i(x)$ depends only on the geometry of the coil i. Practically, $B_{main}(x)$ and $P_i(x)$ are measured by switching on only one coil at a time. It turned out that all fields can be fitted with first or second order polynomials. Writing

$$P_i(x) = a_i x^2 + b_i x + c_i, \tag{2.4}$$

$$B_{main}(x) = Ax^2 + Bx + C, \tag{2.5}$$

the total field becomes

$$B_{total}(x) = \left(\sum_{i=1}^{4} a_i \cdot I_i + A \right) \cdot x^2 + \left(\sum_{i=1}^{4} b_i \cdot I_i + B \right) \cdot x + \left(\sum_{i=1}^{4} c_i \cdot I_i + C \right). \tag{2.6}$$

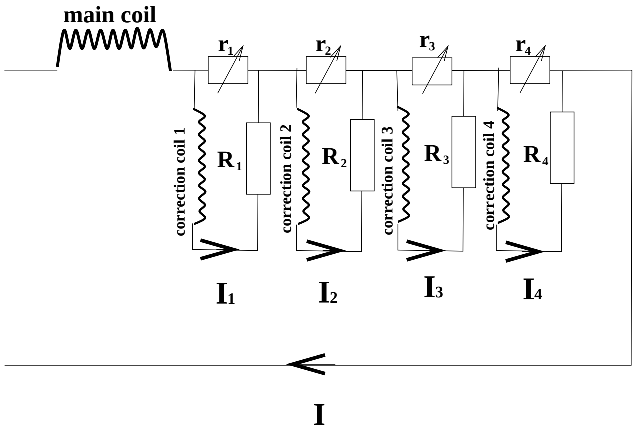

Figure 2.9: Coils current divider

The gradients in the box are removed by setting the potentiometers in a way that the polynomial coefficients vanish.

For this experiment, we decided to minimize $\left(\frac{B_x}{\frac{\partial B_x}{\partial x}}\right)$ and $\left(\frac{B_z}{\frac{\partial B_z}{\partial z}}\right)$. A wide range of currents allows for the minimization of these two gradients.

However, one neglects the z and y dependence of the field components. Moreover, one should also minimize the two other cartesian components of the field with the same four correction coils. It is clear that the degrees of freedom one has to cancel gradients are very restricted. In practice, it is impossible to cancel all gradients with only four coils. The field homogeneity was sufficient to allow for a long target relaxation time but not good enough for NMR measurements which were quite sensitive to magnetic field gradients. This can be seen from fig. 2.10 which shows that the shape of the free induction decay is different from one angle to the other. This is a consequence of an approximate field optimization. As outlined in Appendix-A, a more rigorous approach might partially improve the situation[2].

---

[2] An alternative solution could be a "by hand" optimization of the field. With a polarized cell inside the box, one turns on the potentiometers looking at the free induction decay shape for different angles. Step by step, one can set potentiometers in a way that for the different angles the free induction decay looks similar [45].

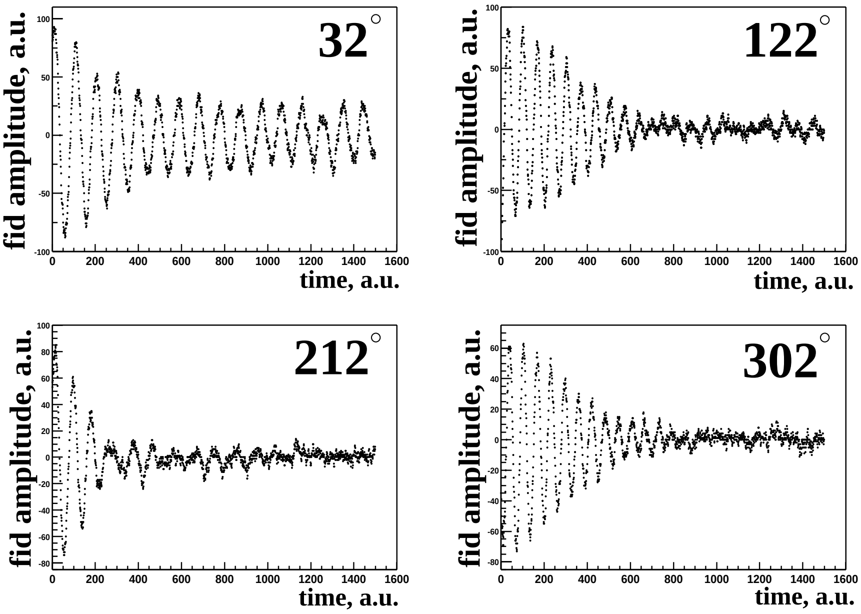

Figure 2.10: Shape of the free induction decay at different spin angles

Chapter 3

Analysis

3.1 Proton detection

3.1.1 Introduction

Because protons are ionizing particles, they deposit a significant amount of energy in the ΔE − paddles. Therefore, protons are events from the upper part of the ADC spectrum of the ΔE − paddles (see fig. 3.1).

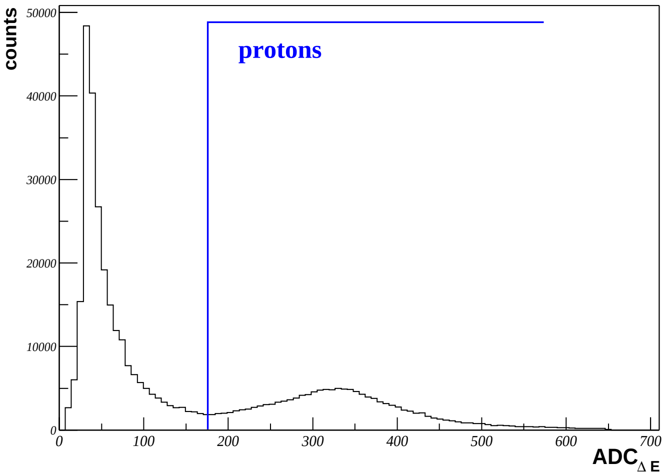

Figure 3.1: ΔE-paddle spectrum with the proton cut

Usually, one defines as protons the events for which two $\Delta E-$ paddles have a large ADC value. A large amount of electromagnetic radiation is produced when the electron beam crosses the target cell copper windows. The low energy electromagnetic background is shielded by lead. However, higher energy showers hit the scintillators, producing sometime a big amount of light which may overlap with "good" events (protons or neutrons). This pile up noise (see appendix-C) produces fake hadron detector-spectrometer coincidences or causes proton misidentifications. For example, neutrons can be detected by the hadron detector with accidentally high noisy pulses on two $\Delta E-$ paddles. Fitting $\Delta E-$ paddles and E-bars pedestals with exponentials, the probability that two $\Delta E-$ paddles and one E-bar accidentally cross the proton threshold can be estimated to be about 1%. To improve the signal to noise ratio, it is necessary to refine the event selection rule.

3.1.2 Proton definition

The electron induces a breakup of the ^3He nucleus. The energy of the outgoing proton is E_p and its momentum is $\vec{p}$, whereas the remaining np system has an energy E_R and a momentum $\vec{p_R}$ given by

$$\vec{p_R} = \vec{q} - \vec{p}. \qquad (3.1)$$

The electron being emitted in rather small solid angle, one can consider that the direction of $\vec{q}$ is constant. This approximation yields

$$|\vec{p_R}|^2 \approx p^2 + q^2 - 2pq \cdot \cos(\Delta\theta_p), \qquad (3.2)$$

where $\Delta\theta_p$ is the proton's in-plane angle relative to $\vec{q}$. The missing energy of the ^3He system is defined by

$$E_m = \omega - E_p - E_R. \qquad (3.3)$$

E_m is below 15MeV with a high probability [46]. Thus, from (3.3), one can calculate the energy of the outgoing proton just after the interaction with the electron, with a few MeV accuracy. On fig. 3.2, E_p is plotted versus ω for different values of the missing energy. In the following, the calculations use $E_m = 8MeV$.

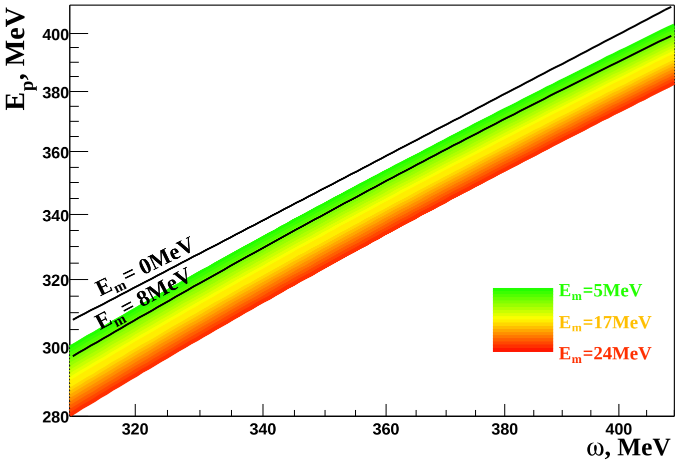

Figure 3.2: E_p versus ω. The calculation use equation (3.3)

After the interaction with the electron, the proton looses energy in different materials. These materials and their thicknesses are listed in tab. 3.1. The copper input in tab. 3.1 corresponds to the 1.1mm thick copper wires which surround the box. These wires are placed every centimeter, vertically and horizontally. At maximum, a proton crosses two wires which represent a thickness of 2.2mm. In addition, bunches of about seven wires, corresponding to the correction coils, are placed on the corner of the box as shown in fig. 3.3. Only protons going towards the left half part of the hadron detector are concerned by these bunches. Assuming that at maximum a proton will cross three of these cables, the maximum copper thickness is 3.3mm.

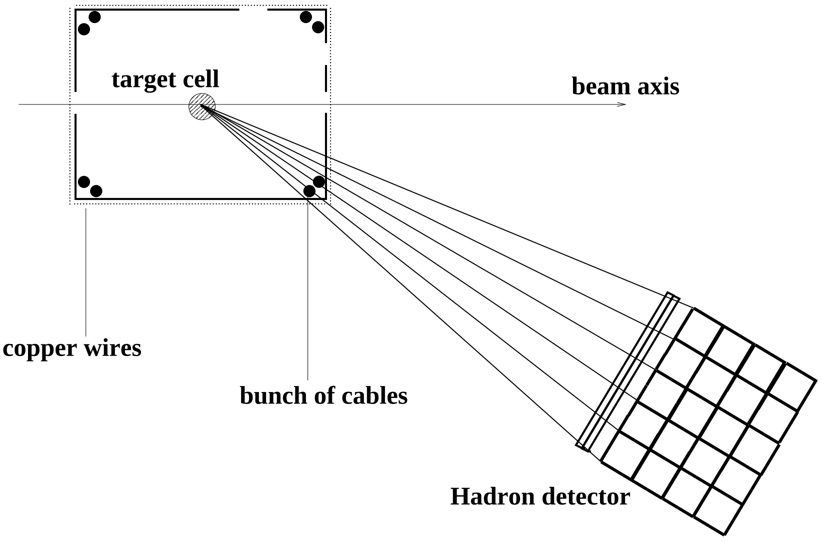

Figure 3.3: Positions of the copper wires used in the energy loss calculations

material	**thickness (cm)**
pyrex	0.2
Copper	0 to 0.33 (random)
μ-metal	0.2
plastic	1.5
iron	0.2
lead	2
plastic	2.6

Table 3.1: Materials and thicknesses crossed by the proton

Because ω is between 300MeV and 410MeV, a valid proton must lose more than 40MeV in at least three adjacent scintillators. Since a bar triggers at 30MeV, valid protons are events with signals above threshold in two consecutive ΔE and in at least 3 bars, as it is shown in fig. 3.4. Such a selection prevents from the $^3\vec{H}e(\vec{e},e'p)\pi X$ reaction where protons have 135MeV less energy and cannot reach the third bar layer. With the additional Cherenkov cut on the electron, one removes almost all noise as it is shown in fig. 3.5.

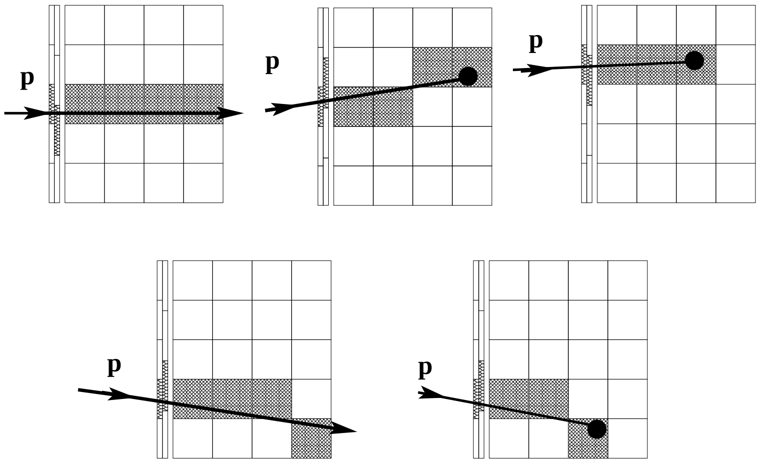

Figure 3.4: Examples of selected events in the hadron detector

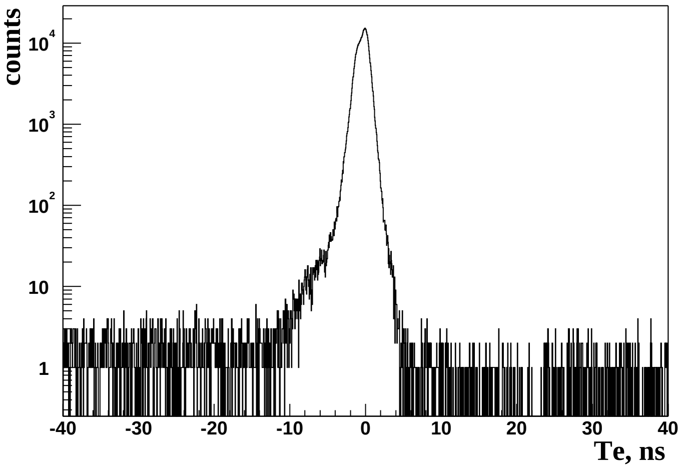

Figure 3.5: T_e after the Cherenkov and proton cuts

From energy loss calculations, one expects that a maximum of energy should be deposited in the last bars of the detector for $\omega \approx 345 MeV$. Fig. 3.6.a and 3.6.b show the energy deposited in the last bars versus ω for a proton angle θ_p=32° and

θ_p=28°, respectively. The copper thickness used in the calculations is indicated near the corresponding line (full lines). These calculations include a $1/\cos(\theta_p)$ correction on the box's wall thickness. The measured ADC spectra have been scaled by a factor 5 in order to fit within the range of the proton's energy loss. This scale factor is the calibration factor of the system [scintillator+PM+electronique].

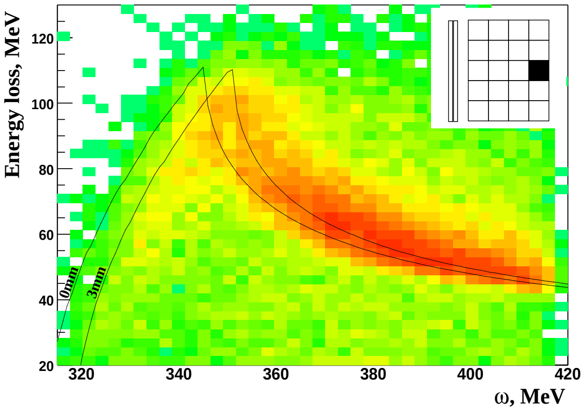

(a) $\theta_p = 32°$

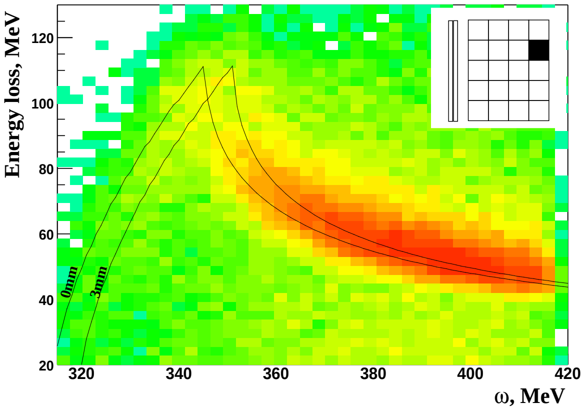

(b) $\theta_p = 28°$

Figure 3.6: Electron equivalent energy loss spectrum versus ω for two bars from the last layer of the hadron detector.

3.1.3 Position measurement

Once the e-p coincidences are selected the segmentation of the detector allows for a measurement of θ, the in-plane polar angle. The resolution on θ, given by the bars thickness, is 3°. To measure the out of plane azimuthal angle ϕ, one needs the vertical position of the proton.

The vertical position of a particle is measured using the propagation time of the light using the TDC information. In principle, it is also possible to use the attenuation the light will undergo when passing through the scintillator as determined by the ADCs. If a proton passes at a distance $X_{u(d)}$ from $PM_{up(down)}$, the time the light needs to reach $PM_{up(down)}$ position is $T_{up(down)} = \frac{X_{u(d)}}{v}$, with v the light velocity inside the bar (v=22cm·ns^{-1} from measurements made at Basel with a light pulser). Thus, the difference between the up and the down TDC is proportional to the proton's position inside the scintillator:

$$TDC_{up} - TDC_{down} = T_{up} - T_{down} = \frac{X_u - X_d}{v} \tag{3.4}$$

Because of light attenuation, an initial quantity of light L_0 emitted towards up(down) side, is measured the on $PM_{up(down)}$ as a quantity of light $L_{u(d)} = L_0 e^{-\frac{X_{u(d)}}{\lambda}}$, with λ the light attenuation coefficient of the scintillator. The ratio of the up and down ADC is in principle proportional to the proton position inside the bar:

$$\frac{ADC_{up}}{ADC_{down}} = e^{-\frac{X_u - X_d}{\lambda}} \approx -\frac{X_u - X_d}{\lambda}. \tag{3.5}$$

However, as outlined in Appendix-B, equation (3.5) is only accurate in the middle of the bar. Moreover, pile up noise spoils the quality of the ADC position measurements. Effects of pile up are treated in Appendix-C. In practice, the level of noise prevents the determination of ϕ with the ADC's.

From the TDC measurements (see Appendix-D), the achieved resolution on ϕ is about 1°.

3.2 Polarization product measurement

For elastic e-^{3}He scattering, the ratio of the measured asymmetry $A^{exp}_{z,x}$ over the theoretical asymmetry $A_{x,z}$ is equal to the product of the beam and target polarization:

$$\frac{A^{exp}_{z,x}}{A_{z,x}} = P_e P_t. \tag{3.6}$$

Since ^3He form factors are experimentally well determined quantities [47], one can calculate the theoretical asymmetry $A_{z,x}$ corresponding to the elastic $^3\vec{H}e(\vec{e},e')^3He$ reaction. On the other hand, $A^{exp}_{z,x}$ is measured using spectrometer B which detects elastically scattered electrons. Thus, one determines P_eP_t through (3.6).

From form factor data, one finds $A_z = (4.47 \pm 0.18)$ and $A_x = (8.07 \pm 0.11)$ for our kinematics [28]. Electrons from the $^3\vec{H}e(\vec{e},e')^3He$ reaction should form a sharp elastic peak at 831MeV in the E' spectrum of spectrometer B. However, the momentum of the electron is not perfectly reconstructed by the spectrometer at this high momentum setting. The deviation from the reference momentum, δp, is reconstructed from the electron focal plan coordinates x, θ, y, ϕ (measured by the VDCs) through

$$\delta p = \sum_{ijkl} a_{ijkl} x^i \theta^j y^k \phi^l. \tag{3.7}$$

The transport matrix elements a_{ijkl} have been determined for 495(MeV/c) electrons [48] (in German). They are not suitable for 831(Mev/c) electrons. To achieve an acceptable momentum resolution at 831(MeV/c), the matrix elements had to be found "by hand". This was done in an iterative process. Additionally, one has also to consider the kinematic peak broadening due to the finite angular acceptance of the spectrometer. An electron of energy E elastically scattered at an angle θ by a nucleus of mass M has an energy E' given by

$$E' = \frac{E}{1 + \frac{2E}{M}\sin^2(\theta/2)}. \tag{3.8}$$

A linear expansion of (3.8) around the central angle $\theta = \theta_0$ gives the correction in θ one has to apply on E' in order to reduce the width of the elastic peak.

Changing the transport matrix and taking into account the kinematical peak broadening, the full width half maximum of the elastic peak is about 900KeV.

The mean polarization product $< P_e P_t >$ measurements are displayed on tab.3.2, together with the polarization product measured using the Møller and AFP-NMR measurements [28]. The mean values for the polarization product are $< P_e P_t >=$

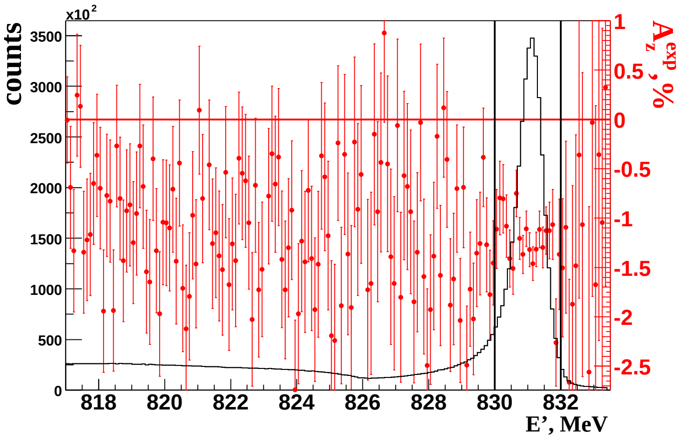

(a) parallel asymmetry

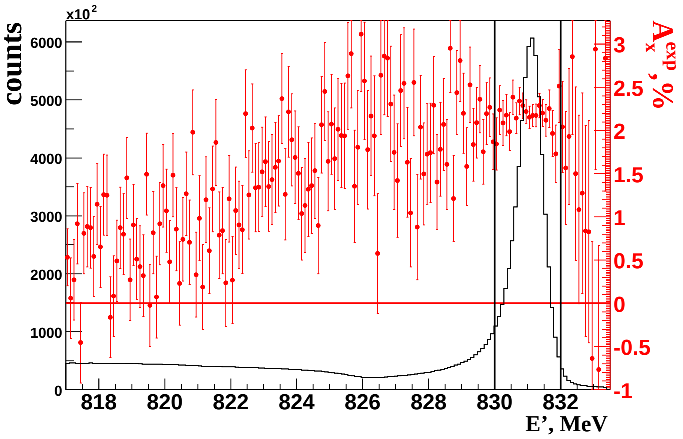

(b) perpendicular asymmetry

Figure 3.7: Scattered electron energy spectra together with asymmetries.

0.2770 ± 0.016 for the parallel spin kinematics and $< P_e P_t >= 0.271 \pm 0.006$ for the perpendicular spin kinematics.

spin angle	$< P_e P_t >$	$< P_e >< P_t >$
0	0.293±0.020	0.294±0.036
90	0.267±0.007	0.287±0.034
180	0.256±0.021	0.264±0.035
270	0.277±0.009	0.278±0.034

Table 3.2: Polarization product measurements for the 4 target spin angles.

Chapter 4

Results and conclusion

4.1 Results

N^+ and N^- are the number of events detected for the electron beam with a helicity +1 and −1, respectively. The measured asymmetry is defined by

$$A = \frac{1}{P_e P_t} \cdot \frac{N^+ - N^-}{N^+ + N^-}. \tag{4.1}$$

In order to study the effect of FSI on the asymmetries in different kinematic regions, the ω spectrum is divided in two regions, labeled 1 and 2 in fig. 4.1. Region 1 covers the peak and therefore emphasizes low nucleon momenta whereas region 2 covers the low ω tail sensitive preferentially to high nucleon momenta. The events in each of the two regions are summed over the entire acceptance of the ou t–of–plane angle of electron and proton and over the electron scattering angle in a range from 75.8^o to 81.8^o.

The measured asymmetries versus the in-plane angle, from regions 1 and 2, are displayed in fig. 4.2 and fig. 4.3, together with calculations made using the AV18 NN-potential [49]. Green full, dot-dot and dot-dashed lines show calculations [50] made with the approximation fig. 1.7, using a non relativistic current operator. The green dot-dash uses non relativistic kinematics, whereas the dot-dot line takes relativistic kinematics into account for the calculations. The blue full and dashed lines show calculations using a relativistic current operator. The full line represents calculations using the approximation of fig. 1.7 (spectator approximation) with relativistic kinematics, and the blue dashed line shows the plane wave impulse approximation (the first diagram of fig. 1.7).

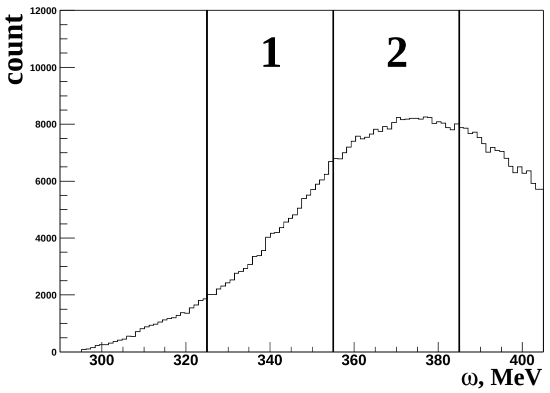

Figure 4.1: Energy transfer spectrum with the two selected regions

The hadron detector does not allow for a high–resolution determination of the proton energy. In particular, it is not possible to distinguish two- and three-body breakup events. Accordingly, the calculations have been integrated over the two-body and over the first 26 MeV of the three-body breakup channel. For the highest accepted missing energy of 26 MeV, the cross section is smaller by at least one order of magnitude compared to the cross section at threshold. Extending the integration limit has no effect on the results. In addition, the calculated results are integrated over the experimentally accepted out–of–plane proton angle and the relevant ω range (fig. 4.1).

With $N^+ \approx N^-$, the standard deviation of a measured asymmetry σ_A is given by

$$\sigma_A^2 = \frac{1}{(P_eP_t)^2} \cdot \frac{1}{N^+ + N^-} + A^2 \left(\frac{\sigma_{P_eP_t}}{P_eP_t} \right)^2 , \tag{4.2}$$

where the first term is the statistical contribution to the total error and the second term is the contribution from polarization measurement uncertainty.

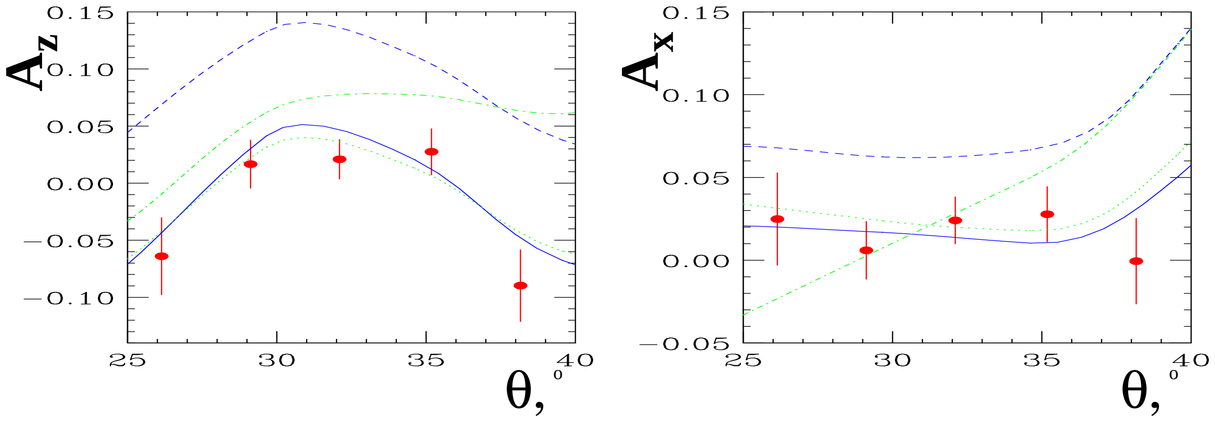

(a) spin parallel asymmetry

(b) spin perpendicular asymmetry

Figure 4.2: Asymmetries integrated over region 2. The results of the full(PWIA) calculations are shown in blue full(dashed). The result of a full calculation using a non-relativistic current with relativistic kinematics (green dot) and with non-relativistic kinematics (green dot-dashed) are also shown.

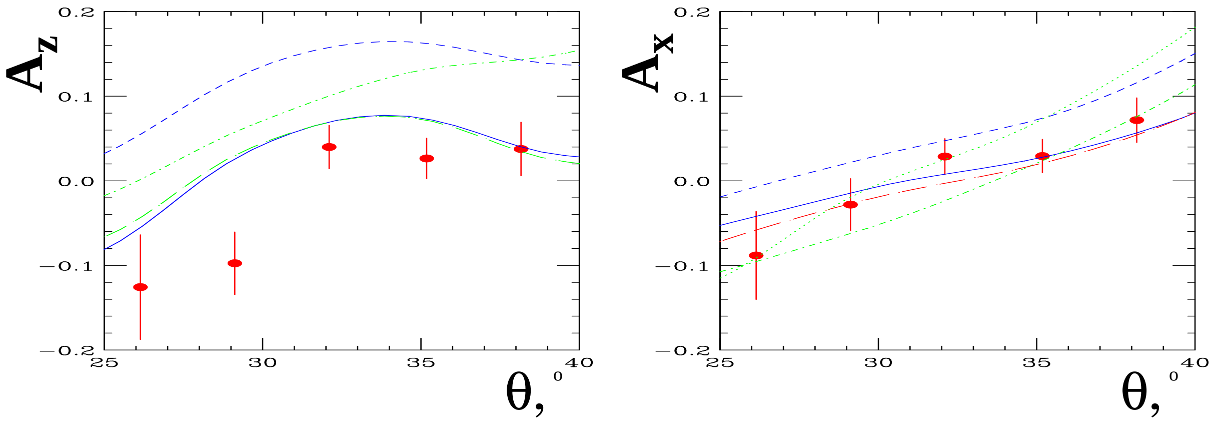

(a) spin parallel asymmetry

(b) spin perpendicular asymmetry

Figure 4.3: Same as figure 4.2 but for an integration over region 1.

Since the coincidence peak shown in fig. 3.5 is almost background free, there are no corrections due to noise.

In the tail of the protons angular distribution, where statistics are low, the first term of equation (4.2) is in absolute typically about $1{\cdot}10^{-3}$ to $2{\cdot}10^{-3}$, whereas the second term is about $2{\cdot}10^{-4}$ for parallel kinematics and 10^{-5} for perpendicular kinematics. Thus, uncertainties are mainly statistical.

4.2 Discussion

Fig. 4.2 and fig. 4.3 show that the PWIA calculations are in clear disagreement with the experimental results. The same holds for the calculation which does not account for relativistic kinematics. On the other hand, very good agreement between experiment and theory is found using the spectator approximation and accounting for relativistic kinematics. This applies also for the results using the CD–Bonn NN–potential with negligible differences. Small differences of the results are observed when the current is replaced by a non–relativistic version and also when a relativistic $(v/c)^2$–correction is added. The results indicate that at high Q^2, where completely non–relativistic calculations are not applicable anymore, a good description of the data can be achieved taking into account relativistic kinematics and an approximate treatment of FSI–effects. The use of a relativistic current operator is less relevant.

This result is important for experiments aimed at extracting quantitative properties of the neutron from asymmetry measurements of inclusive $^3\vec{H}e(\vec{e}, e')$ or exclusive $^3\vec{H}e(\vec{e}, e'n)$ reactions. The corrections for FSI–effects concerning the rescattering effect can be reliably calculated within the approach presented here.

The effect of the rescattering process on asymmetries measured in $^3\vec{H}e(\overrightarrow{e}, e'n)$ is less important than in $^3\vec{H}e(\overrightarrow{e}, e'p)$. It is interresting to notice that the situation is reversed for the charge exchange contribution due to the fact that the electron interacts preferentially with the protons.

4.3 Conclusion

Concerning the 2003 experiment, aiming to measure G_e^n at Q^2=0.67(GeV/c)^2, the correction coming from the rescattering process amounts to 0.4% of the measured value of G_e^n. On the other hand, the correction coming from charge exchange introduces 3% correction on G_e^n [26]. Taking the rescattering and charge exchange processes together, one has to correct G_e^n by 3.4% at Q^2=0.67(GeV/c)^2.

Appendix A

Magnetic field optimization

Having in hand the analytic form of the magnetic fields, one knows what is reasonable to expect when trying to minimize the gradients. And above all, one knows what is impossible to do. Thus, one could avoid to spend time in blindly turning potentiometers with the hopeless goal to reach a "perfect" magnetic field. The efficiency and reliability of the following analytic approach were not completely investigated. Since I think it could be worthwhile to use this method in the future, I add the following appendix in my thesis.

Lets consider the z and x components of the magnetic field associated with one of the 2 main coils X or Z (fig. 2.8):

$$\overrightarrow{\mathbf{B}}\left(\mathrm{x},\mathrm{z}\right)=\left(\mathrm{B}_{\mathrm{x}}\left(\mathrm{x},\mathrm{z}\right);\mathrm{B}_{\mathrm{z}}\left(\mathrm{x},\mathrm{z}\right)\right). \tag{A.1}$$

A coil i, to which a current I^i is applied, produces a magnetic field $\overrightarrow{\mathbf{B^i}}\left(\mathrm{x},\mathrm{z}\right)=\left(\mathrm{B}^{\mathrm{i}}_{\mathrm{x}}\left(\mathrm{x},\mathrm{z}\right);\mathrm{B}^{\mathrm{i}}_{\mathrm{z}}\left(\mathrm{x},\mathrm{z}\right)\right)$. Lets assume its cartesian components are

$$B_x^i\left(x,z\right)=\left(b_x^i+C_x^i\cdot x+D_x^i\cdot z+F_x^i\cdot z^2+G_x^i\cdot xz\right)\cdot I^i, \tag{A.2}$$

and

$$B_z^i\left(x,z\right)=\left(b_z^i+C_z^i\cdot x+D_z^i\cdot z+F_z^i\cdot z^2+G_z^i\cdot xz\right)\cdot I^i. \tag{A.3}$$

In (A.2) and (A.3), i=0 for the main coil, and $i \in \{1, 2, 3, 4\}$ for the correction coils. The static field is measured when all coils are switched off. Its components are

$$B_x^{static}(x,z) = b_x^{static} + C_x^{static} \cdot x + D_x^{static} \cdot z + F_x^{static} \cdot z^2 + G_x^{static} \cdot xz, \quad \text{(A.4)}$$

and

$$B_z^{static}(x,z) = b_z^{static} + C_z^{static} \cdot x + D_z^{static} \cdot z + F_z^{static} \cdot z^2 + G_z^{static} \cdot xz. \quad \text{(A.5)}$$

The measurements one has to do to get the coefficients C_x^i, D_x^i, F_x^i and G_x^i are quite tedious. Indeed, one has to move the field probe through holes made in the box to let the scattered electrons pass. In the experimental hall, the available place to do such measurements is quite restricted. For each coil, one has to measure the field at different positions on the (x, z) plan, not only along the axis of the box, but also on some off-axis position as it is shown in fig. A.1 for example. However, such measurements have to be done only one time. Since the shape of the coils and the box are not changing, the effect of the coils is always the same. In practice, only remains the measurement of the static field which may change from one target's environment to the other. The currents passing through a correction coil being proportional to the main current I^0, one can write all currents in the form $I^i = \alpha_i \cdot I^0$, with $\alpha_0 = 1$ and $\alpha_{i \neq 0}$ being given by the potentiometers set. The sum of the fields gives:

$$B_x(x,z) = \sum_{i=0}^{4} \alpha_i b_x^i + b_x^{static} + x\left(\sum_{i=0}^{4} \alpha_i \frac{C_x^i}{I_0} + C_x^{static}\right) + z\left(\sum_{i=0}^{4} \alpha_i \frac{D_x^i}{I_0} + D_x^{static}\right)$$
$$+x^2\left(\sum_{i=0}^{4} \alpha_i \frac{E_x^i}{I_0} + E_x^{static}\right) + z^2\left(\sum_{i=0}^{4} \alpha_i \frac{F_x^i}{I_0} + F_x^{static}\right) + xz\left(\sum_{i=0}^{4} \alpha_i \frac{G_x}{I_0} + G_x^{static}\right), \quad \text{(A.6)}$$

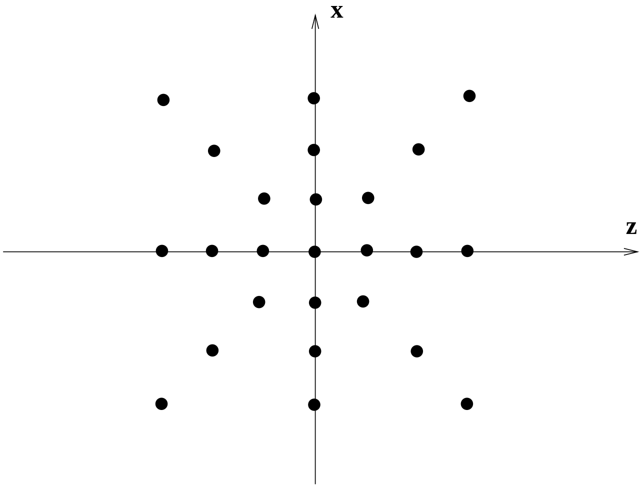

Figure A.1: Positions where one could measure the field to do the correction properly

and

$$B_z(x,z) = \sum_{i=0}^{4} \alpha_i b_z^i + b_z^{static} + x\left(\sum_{i=0}^{4} \alpha_i \frac{C_z^i}{I_0} + C_z^{static}\right) + z\left(\sum_{i=0}^{4} \alpha_i \frac{D_z^i}{I_0} + D_z^{static}\right)$$
$$+x^2\left(\sum_{i=0}^{4} \alpha_i \frac{E_z^i}{I_0} + E_z^{static}\right) + z^2\left(\sum_{i=0}^{4} \alpha_i \frac{F_z^i}{I_0} + F_z^{static}\right) + xz\left(\sum_{i=0}^{4} \alpha_i \frac{G_z}{I_0} + G_z^{static}\right). \tag{A.7}$$

Our goal is to get B_z and B_x independent of x and z, "as much as possible". This can be achieved if all the polynomial coefficients in (A.6) and (A.7) are set to zero. These coefficients being linear with α_i, the solution to our problem is given by 10 linear equations. With the 4 degrees of freedom given by $\{\alpha_i\}_{i\in\{1,2,3,4\}}$ it is impossible to solve simultaneously all these equations.

One approach could be to minimize a quantity of the kind

$$\left(\sum_{i=0}^{4} \alpha_i \frac{C_x^i}{I_0} + C_x^{static}\right)^2 + \cdots + A\sum_{i=1}^{4}\left(\frac{\alpha_i}{\alpha_{max}}\right)^2, \tag{A.8}$$

where α_{max} and A are factors giving the magnitude of the constraint «α_i should be as small as possible» (realistic potentiometer setting). The bigger these factors, the farer we end from the optimal solution, but the lesser the demand on the potentiometers. This last condition might be important to avoid any overheating of the potentiometers. The least square solution of (A.8) brings one to solve a linear system in $(\alpha_1; \alpha_2; \alpha_3; \alpha_4)$.

Appendix B

Edge effect

B.1 Qualitative understanding

Fig. B.1 reveals the nonlinearity of position measurements done with ADCs near the sides of the bar. A BC400 scintillator has a reflection index $n_1 = 1.58$, whereas air has a reflection index $n_2 = 1$. If a ray of light, produced somewhere in the scintillator, hits the air-scintillator surface with an angle i_1, it is refracted

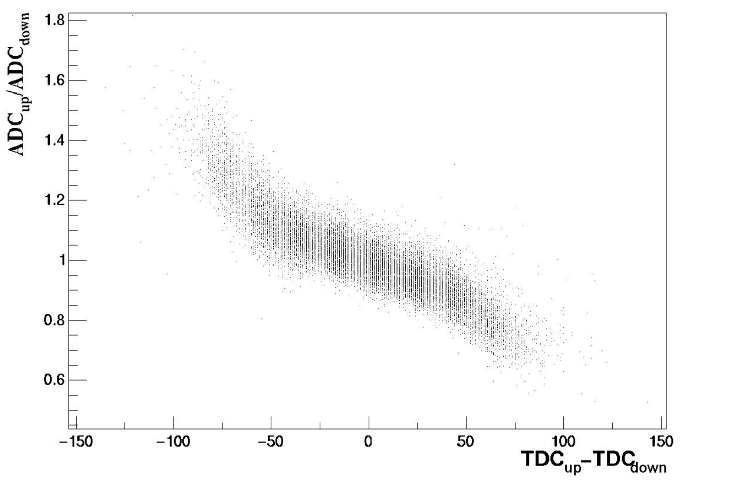

Figure B.1: ADC ratio versus TDC difference of PMs from the same bar

outside the bar with an angle i_2 given by the well known Snell-Descartes relation:

$$n_1 \sin(i_1) = n_2 \sin(i_2) \tag{B.1}$$

i_2 exists if and only if

$$i_1 < Asin\frac{n_2}{n_1} = i_0 = 40^o \tag{B.2}$$

If (B.2) is not fullfilled ($i_1 > i_0$) the ray cannot escape from the scintillator, it is totally reflected. After many reflections, such a ray reaches one of the sides of the bar and is finally seen by the PM (rays R_1 and R_2 in fig. B.2). However, if $i_1 \leq i_0$, the ray goes outside the scintillator, it is lost (ray R_{-1} in fig. B.2). When

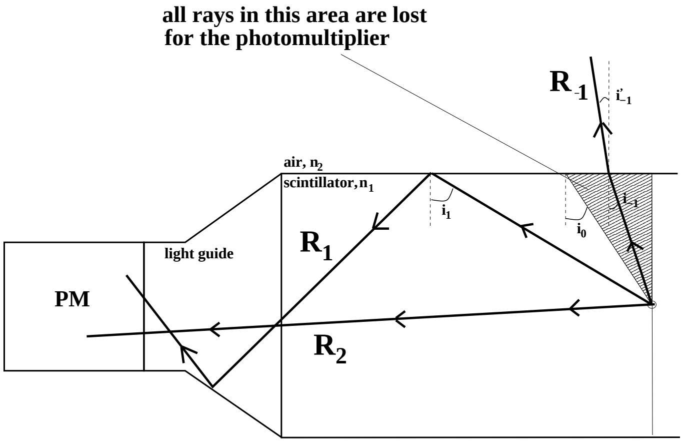
all rays in this area are lost
for the photomultiplier

Figure B.2: Light propagation in the scintillator

the source of light is very near to one of the sides, part of the rays which should escape the scintillator ($i_1 \leq i_0$) is seen directly by the PM without undergoing any reflection on the bar surface : the initial quantity of light sent towards the nearest PM is bigger than the one sent towards the farest PM (fig. B.3).

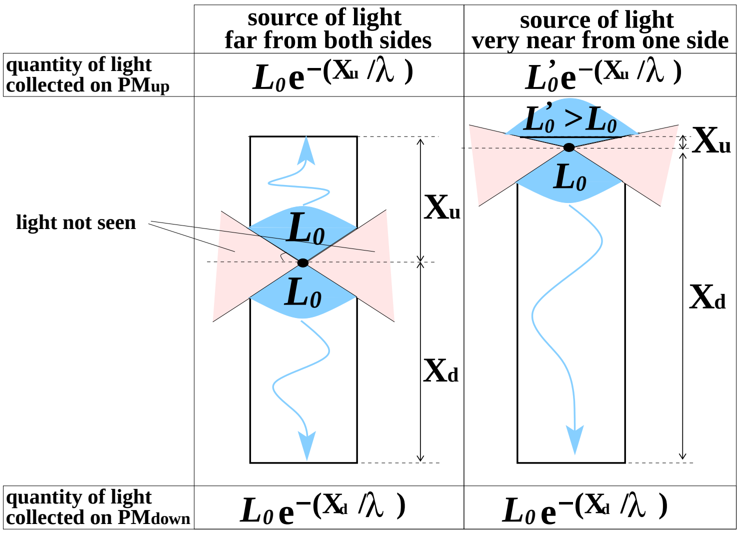
source of light far from both sides
source of light very near from one side
quantity of light collected on PMup
L0 e−(Xu /λ)
L'0 e−(Xu /λ)
L'0 >L0
L0
L0
L0
Xu
Xu
light not seen
Xd
Xd
quantity of light collected on PMdown
L0 e−(Xd /λ)
L0 e−(Xd /λ)

Figure B.3: Edge effect in the light collection

B.2 Quantitative understanding

Let's consider a proton which passes through a bar at position x=X. The center of the bar is the origin of the axis system shown in fig. B.4. The path of the proton inside the bar defines a segment from which the scintillation light is isotropically produced. This segment is defined by $\{x=X;y\in [\frac{-d}{2};\frac{d}{2}];z=0\}$, with $X\in [\frac{-D}{2};\frac{+D}{2}]$. Some rays are internally reflected in the scintillator and reach one of the two surfaces S+ or S−. If a ray escapes the scintillator, it is not seen by the PM in S+ or S−. However, the scintillators are covered with aluminium foils. Thus, there is a probability U that the ray gets reflected on the aluminium surface and reenters the scintillator with a random direction. The path of a ray can be described by the algorithm fig. B.5. The quantity of interest is the number $n_i^{+(-)}$ of rays which cover a distance l_i before reaching S+(−). With λ the scintillator attenuation lengh, a PM at position +(−) gives a signal proportional to

$$L_{+(-)} = \sum_i n_i^{+(-)} e^{-l_i^{+(-)}/\lambda}. \tag{B.3}$$

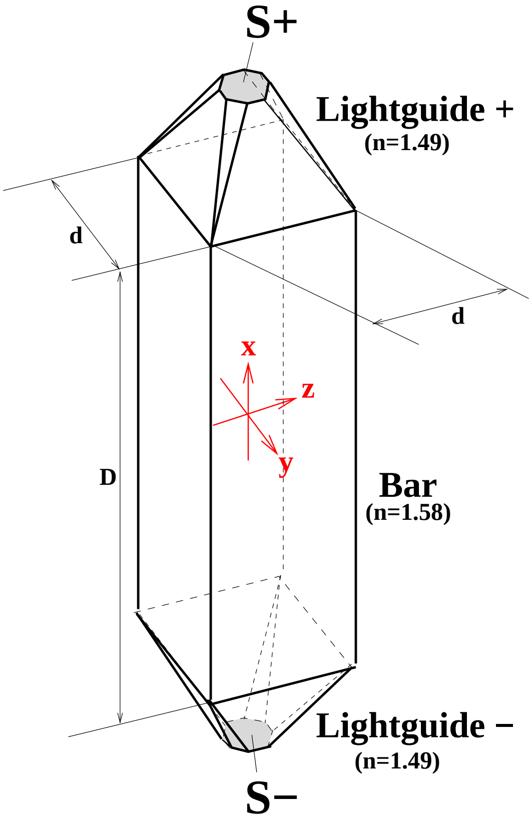

Figure B.4: Scintillator with the definition of the axis.

The distribution of l_i for X=0cm and X=20cm is shown in red in fig. B.6.a and fig. B.6.b respectively, with U=0.9. The black distribution takes the attenuation lengh λ=160cm into account. In fig. B.7, one sees the experimental distribution of the ADCs ratio versus the TDCs difference. The factor $\frac{1}{1.1}$ converts the TDC channels into centimeters (1 TDC channel=0.05ns with a speed of light v=22cm.ns^{-1}). Are also shown results of simulations using different U and λ.

With U$\approx$0.9 and $\lambda \approx$160cm, one describes well the global behavior of the ADCs ratio versus X. These values are consistant with the known aluminium reflectivity in the ultraviolet range and with BC400 scintillators light attenuation lenght. The effective value of λ (which is given by the slope of the ADCs ratio versus the TDCs difference) is about 320cm. Accordingly, one can define an effective attenuation lengh λ_{eff}=320cm which depends on the geometry of the scintillator.

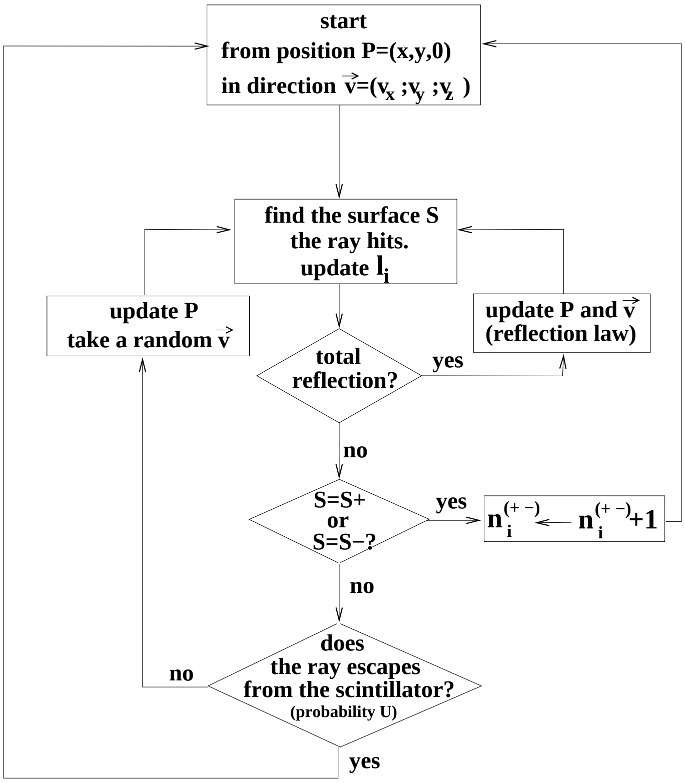
start
from position P=(x,y,0)
in direction v=(vx ;vy ;vz)
find the surface S
the ray hits.
update li
update P
take a random v
update P and v
(reflection law)
total
reflection?
yes
no
S=S+
or
S=S−?
yes
ni(+ −) ← ni(+ −)+1
no
does
the ray escapes
from the scintillator?
(probability U)
no
yes

Figure B.5: Algorithm describing the path of the light inside the scintillator.

$\frac{L_+}{L_-}(X)$ bends quite a lot near the sides of the bar. Such a bending can hardly be guessed from the measurements in fig. B.7. Fig. B.8 indicates that this effect comes mainly from absorption in the lightguides. In fig. B.8 the "lost by attenuation" corresponds to a cut-off made on rays which travel more than 900cm (with λ =160cm, such rays can be neglected). For U=1, the small remaining bending effect comes from rays which are coming back from the opposite side of the bar.

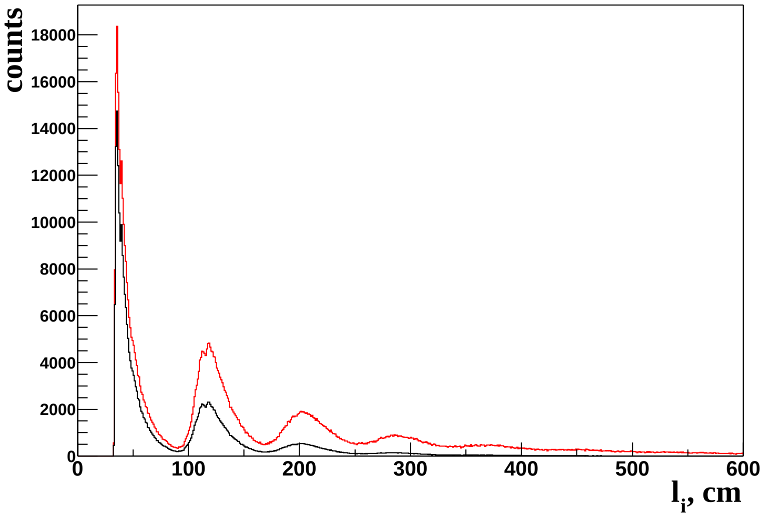

(a) X=0cm

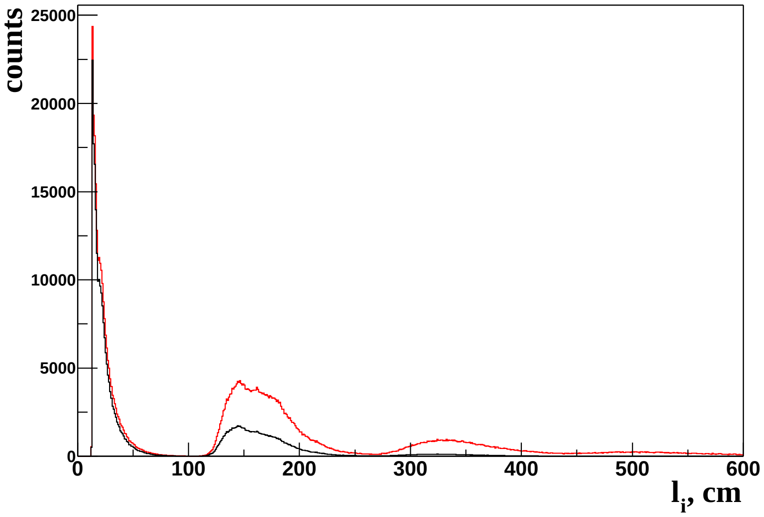

(b) X=20cm

Figure B.6: Path lengh distribution of a ray that reaches S+, without light attenuation (red) and with light attenuation (black).

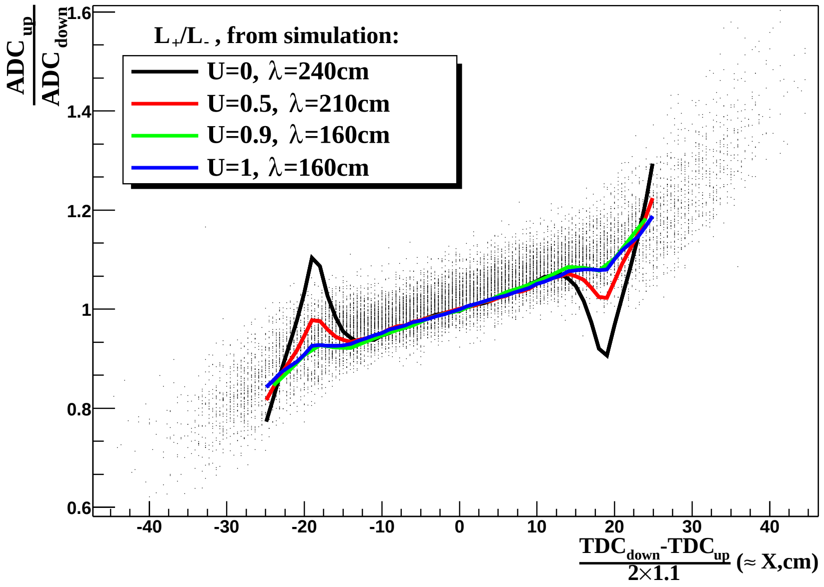

Figure B.7: Comparison of the measured ADCs ratio shape with simulations.

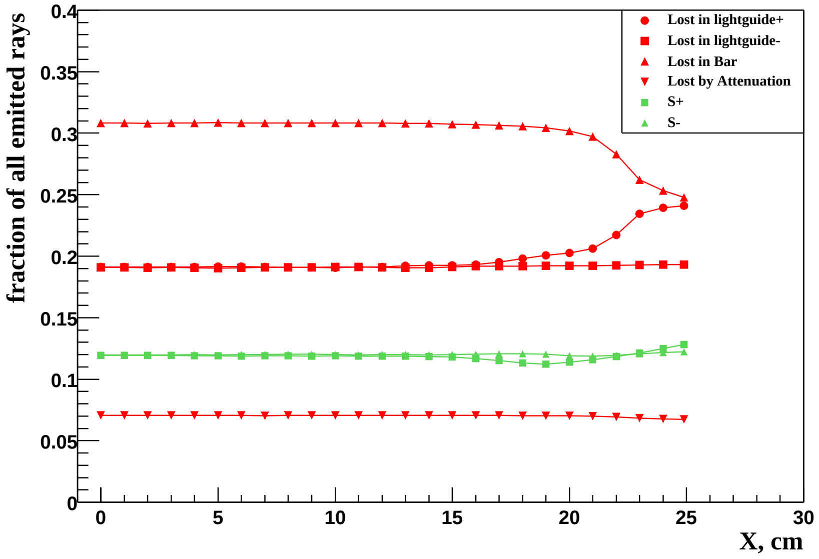

Figure B.8: Probabilities to lose a ray (red curves) and to detect a ray (green curves) versus the position of the proton in the bar, with U=0.5.

Appendix C

Pile up and position measurement

Here I address the problem of finding the resolution on the position measurement, when it is measured with ADCs in presence of pile up noise.

A proton hits the scintillator bar at position X and deposits an energy E. The bar has a total length D and attenuation coefficient λ. One measures $ADC_{up} = \alpha_{up} E e^{-\frac{D+X}{2\lambda}}$ for PM$_{up}$ and $ADC_{down} = \alpha_{down} E e^{-\frac{D-X}{2\lambda}}$ for PM$_{down}$. With $\lambda >> X$, one recovers the position using the ratio r of the 2 ADC measurements:

$$r = \frac{ADC_{up}}{ADC_{down}} \approx \frac{\alpha_{up}}{\alpha_{down}} \cdot \left(1 - \frac{X}{\lambda}\right) \tag{C.1}$$

In principle, the calibration factors α_{up} and α_{down} are reachable after a calibration of the system [scintillator+PM+electronique]. However, in (C.1), only the ratio $\frac{\alpha_{up}}{\alpha_{down}}$ is relevant. Such a ratio is given by a linear fit of ADC_{up} versus ADC_{down}.

Let's investigate the effect of a photon which interacts somewhere in the scintillator, at the same time the proton does (within the ADC integration window). Such a photon deposits an energy ε at a position x. The ratio of the 2 ADCs becomes:

$$r = \frac{ADC_{up}}{ADC_{down}} = \frac{\alpha_{up}}{\alpha_{down}} \cdot \frac{E e^{-\frac{D-X}{2\lambda}} + \varepsilon e^{-\frac{D-x}{2\lambda}}}{E e^{-\frac{D+X}{2\lambda}} + \varepsilon e^{-\frac{D+x}{2\lambda}}}. \tag{C.2}$$

From (C.2), with $\widehat{r} = r \cdot \frac{\alpha_{down}}{\alpha_{up}}$, $\lambda >> X$ and $\lambda >> x$, one gets:

$$X = \frac{\widetilde{r}-1}{\widetilde{r}+1} \cdot (2\lambda + D) + \frac{\varepsilon}{E}\left((2\lambda + D) \cdot \frac{\widetilde{r}-1}{\widetilde{r}+1} - x\right). \tag{C.3}$$

ε and x are two random quantities. One gets the probability distribution of ε through the pedestal spectrum of the bar which presently can be fitted with an exponential. Since the probability density function of ε is an exponential law $\varepsilon_0 e^{-\frac{\varepsilon}{\varepsilon_0}}$, its mean value $< \varepsilon >$ and variance σ_ε^2 are equal to ε_0 and ε_0^2 respectively. Typically, ε_0=17 ADC channels. Assuming that x is uniformly distributed between $-\frac{D}{2}$ and $+\frac{D}{2}$, its mean value is 0 and its variance is $\sigma_x^2 = \frac{D^2}{12}$.

Given the measurement of $\widetilde{r}$, the best estimate of X is:

$$\hat{X} = \frac{\widetilde{r}-1}{\widetilde{r}+1} \cdot (2\lambda + D) + \frac{< \varepsilon >}{E}\left((2\lambda + D) \cdot \frac{\widetilde{r}-1}{\widetilde{r}+1}\right). \tag{C.4}$$

After many measurements, (C.4) insures that the mean error on X is null. The resolution on X is [1]:

$$\sigma_X^2 = \frac{\sigma_\varepsilon^2}{E^2}\left((2\lambda + D) \cdot \frac{\widetilde{r}-1}{\widetilde{r}+1}\right)^2 + \frac{< \varepsilon^2 >}{E^2} \cdot \sigma_x^2. \tag{C.5}$$

The dependence of σ_X versus $\widetilde{r}$ is shown in fig. C.1.

From fig. C.1, one sees that σ_X increases quite a lot as soon as $\widetilde{r}$ goes away from 1: in presence of pile up, ADCs are not a very useful help for accessing the position of the proton in a scintillator. It is also interresting to note that the distribution of the errors becomes less and less symmetric when $\widetilde{r}$ becomes different from 1. Shapes of the error distribution are shown in fig. C.2 (simulation).

---

[1] If one chooses to ignore pile up, then, in (C.4), one has to replace $< \varepsilon >$ by 0 (maximum likelihood solution). Then, the resolution on X is given by ${\sigma_X^2}' =< \varepsilon^2 > \left(\frac{1}{E^2}\left((2\lambda + D) \cdot \frac{\widetilde{r}-1}{\widetilde{r}+1}\right)^2 + \frac{1}{E^2} \cdot \sigma_x^2\right) > \sigma_X^2$, σ_X^2 being defined by (C.5).

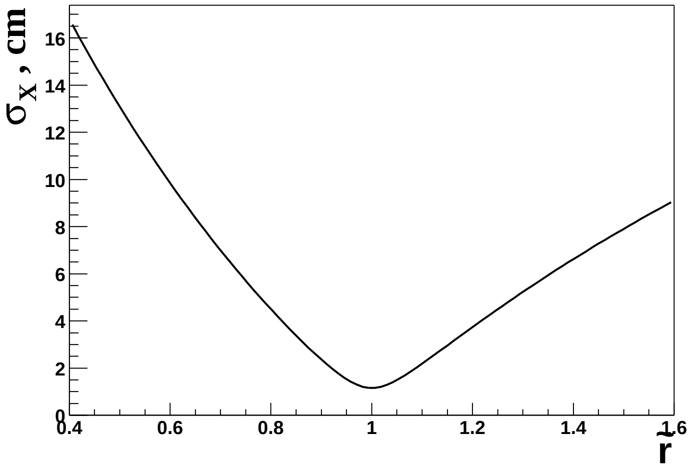

Figure C.1: σ_X versus $\tilde{r}$, with E=300 ADC channels, D=50cm and $\lambda = 320cm$.

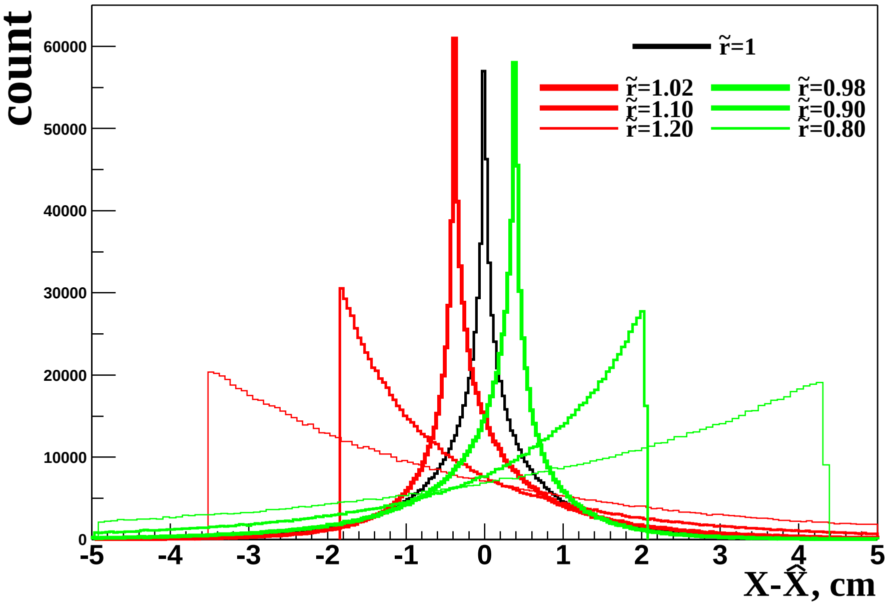

Figure C.2: Error distribution for different values of $\tilde{r}$

Appendix D

Optimal combination of measurements

Let's consider a random quantity D of variance σ_D^2 that one would like to estimate by means of n independent measurements. One measurement E_i gives D with a random error e_i the variance σ_i^2 of which is known:

$$E_i = D + e_i. \tag{D.1}$$

Our goal is to combine the E_i in an optimal way and to find the $\{\alpha_i\}_{i\in\{1,\cdots,n\}}$ minimizing the variance σ_e^2 of the error e (D.2).

$$e = \sum_{i=1}^{n} \alpha_i E_i - D. \tag{D.2}$$

σ_e^2 is given by

$$\sigma_e^2 = \sum_{i=1}^{n} \alpha_i^2 \sigma_i^2 + \left(\sum_{i=1}^{n} \alpha_i^2 - 1 \right) \sigma_D^2, \tag{D.3}$$

provided that :

- $< D >= 0$
- $< e_i >= 0 \ \forall i \in \{1, \cdots, n\}$

- $< e_i \cdot e_j >= 0\ \forall i \neq j$ (independent errors)
- $< e_i \cdot D >= 0\ \forall i \in \{1, \cdots, n\}$ (errors independent of D)

A least square minimization of σ_e^2 relative to $\{\alpha_i\}_{i\in\{1,\cdots,n\}}$ gives the linear system:

$$\left\{\begin{array}{c} \alpha_1(\sigma_1^2+\sigma_D^2)+\alpha_2\sigma_2^2+\cdots+\alpha_n\sigma_n^2=\sigma_D^2 \\ \alpha_1\sigma_1^2+\alpha_2(\sigma_2^2+\sigma_D^2)+\cdots+\alpha_n\sigma_n^2=\sigma_D^2 \\ \cdots \\ \alpha_1\sigma_1^2+\alpha_2\sigma_2^2+\cdots+\alpha_n(\sigma_n^2+\sigma_D^2)=\sigma_D^2 \end{array}\right\} \tag{D.4}$$

$\{\alpha_i\}_{i\in\{1,\cdots,n\}}$, solution of (D.4), is given by

$$\alpha_i = \frac{\frac{1}{\sigma_i^2}}{\frac{1}{\sigma_1^2}+\frac{1}{\sigma_2^2}+\cdots+\frac{1}{\sigma_n^2}+\frac{1}{\sigma_D^2}}, \tag{D.5}$$

leading to an optimal resolution

$$\sigma_e^2 = \frac{1}{\frac{1}{\sigma_1^2}+\frac{1}{\sigma_2^2}+\cdots+\frac{1}{\sigma_n^2}+\frac{1}{\sigma_D^2}}. \tag{D.6}$$

Another way to obtain (D.5) and (D.6) is to consider the case where both e_i and D follows gaussian laws with respective variances σ_i^2 and σ_D^2. Using Baye's law, with $P(A|B)$ standing for "probability of having A knowing B", one gets :

$$P(D|E_1,\cdots,E_n) = \frac{P(E_1,\cdots,E_n|D)\cdot P(D)}{P(E_1,\cdots,E_n)} \tag{D.7}$$

Given the independence of all measurements,

$$P(D|E_1,\cdots,E_n) = \frac{e^{-\frac{(E_1-D)^2}{2\sigma_1^2}}\cdots e^{-\frac{(E_n-D)^2}{2\sigma_n^2}}\cdot e^{-\frac{D^2}{2\sigma_D^2}}}{P(E_1,\cdots,E_n)}, \tag{D.8}$$

with

$$P(E_1,\cdots,E_n) = \int_{-\infty}^{+\infty} e^{-\frac{(E_1-D)^2}{2\sigma_1^2}}\cdots e^{-\frac{(E_n-D)^2}{2\sigma_n^2}}\cdot e^{-\frac{D^2}{2\sigma_D^2}}dD, \tag{D.9}$$

(D.8) can be written in the form

$$P(D|E_1,\cdots,E_n) = \frac{1}{\sqrt{2\pi}\sigma_e}e^{-\left(D-\sigma_e^2\sum_{i=1}^{n}\frac{E_i}{\sigma_i^2}\right)^2 / 2\sigma_e^2}, \tag{D.10}$$

where σ_e is given by (D.6). (D.5) and (D.6) correspond respectively in (D.10) to the posterior mean value and the posterior variance of D, given the measurements $\{E_1, \cdots, E_n\}$.

One gets σ_i and σ_ϕ using correlation coefficients $\mathcal{C}_{ij} = \frac{1}{N}\sum_{m=1}^{N} \phi_i^m \phi_j^m$, N being the total number of measurements. Indeed, writing $\phi_i = \phi + e_i$, e_i being the measurement error, $\mathcal{C}_{ij}$ can be put in the form (D.11), where <X> stands for the mean value of X.

$$\mathcal{C}_{ij} = <\phi^2> + <e_i \cdot e_j> + \phi\,(<e_i> + <e_j>) \tag{D.11}$$

Since $<e_i> = 0$ for any i, and assuming that e_i and e_j are independent, $\mathcal{C}_{ij}$ becomes:

$$\mathcal{C}_{ij} = \sigma_\phi^2 + \delta_{ij} \cdot \sigma_i^2 \tag{D.12}$$

Building the covariance matrix $\mathcal{C}$ of the measurements, one finds $\sigma_i^2 + \sigma_\phi^2$ on the diagonal elements and σ_ϕ^2 on the nondiagonal elements. For instance, (D.13) to (D.17) give covariance matrices formed with protons passing through different set of bars, as well as σ_ϕ and the resolutions $\sigma_{1,2,3,4}$ associated with the different PM pairs.

$$\mathcal{C}_{-2} = \begin{pmatrix} 130.84 & 120.00 & 120.77 & 121.06 \\ 120.00 & 120.90 & 116.97 & 117.56 \\ 120.77 & 116.97 & 128.36 & 120.89 \\ 121.06 & 117.56 & 120.89 & 127.80 \end{pmatrix}_{(▦)} \Rightarrow \sigma_\Phi = 10.93^\circ \pm 0.15, \begin{cases} \sigma_1 = 3.4^\circ \pm 0.4^\circ \\ \sigma_2 = 1.2^\circ \pm 1.1^\circ \\ \sigma_3 = 3.0^\circ \pm 0.4^\circ \\ \sigma_4 = 2.9^\circ \pm 0.4^\circ \end{cases} \tag{D.13}$$

$$\mathcal{C}_{-1} = \begin{pmatrix} 121.72 & 115.88 & 113.11 & 113.11 \\ 115.88 & 117.88 & 112.88 & 112.82 \\ 113.11 & 112.88 & 116.61 & 114.29 \\ 113.11 & 112.82 & 114.29 & 127.26 \end{pmatrix}_{(▦)} \Rightarrow \sigma_\Phi = 10.66^\circ \pm 0.95, \begin{cases} \sigma_1 = 2.8^\circ \pm 1.1^\circ \\ \sigma_2 = 2.0^\circ \pm 1.6^\circ \\ \sigma_3 = 1.7^\circ \pm 1.9^\circ \\ \sigma_4 = 3.7^\circ \pm 0.9^\circ \end{cases} \tag{D.14}$$

$$\mathcal{C}_0 = \begin{pmatrix} 129.32 & 112.03 & 112.82 & 110.31 \\ 112.03 & 116.47 & 111.65 & 109.77 \\ 112.82 & 111.65 & 118.33 & 112.11 \\ 110.31 & 109.77 & 112.11 & 114.53 \end{pmatrix}_{\text{(▦)}} \Rightarrow \sigma_\Phi = 10.56^\circ \pm 0.10, \begin{cases} \sigma_1 = 4.2^\circ \pm 0.2^\circ \\ \sigma_2 = 2.2^\circ \pm 0.5^\circ \\ \sigma_3 = 2.6^\circ \pm 0.4^\circ \\ \sigma_4 = 1.8^\circ \pm 0.6^\circ \end{cases} \tag{D.15}$$

$$\mathcal{C}_{+1} = \begin{pmatrix} 122.59 & 112.23 & 110.34 & 111.81 \\ 112.23 & 113.67 & 108.79 & 110.75 \\ 110.34 & 108.79 & 111.54 & 111.27 \\ 111.81 & 110.75 & 111.27 & 119.57 \end{pmatrix}_{\text{(▦)}} \Rightarrow \sigma_\Phi = 10.53^\circ \pm 0.11, \begin{cases} \sigma_1 = 3.4^\circ \pm 0.3^\circ \\ \sigma_2 = 1.7^\circ \pm 0.6^\circ \\ \sigma_3 = 0.8^\circ \pm 1.3^\circ \\ \sigma_4 = 3.0^\circ \pm 0.4^\circ \end{cases} \tag{D.16}$$

$$\mathcal{C}_{+2} = \begin{pmatrix} 154.56 & 127.35 & 128.62 & 125.27 \\ 127.35 & 127.84 & 125.05 & 122.29 \\ 128.62 & 125.05 & 136.95 & 125.49 \\ 125.27 & 122.29 & 125.49 & 130.33 \end{pmatrix}_{\text{(▦)}} \Rightarrow \sigma_\Phi = 11.21^\circ \pm 0.18, \begin{cases} \sigma_1 = 5.4^\circ \pm 0.3^\circ \\ \sigma_2 = 1.5^\circ \pm 1.0^\circ \\ \sigma_3 = 3.4^\circ \pm 0.4^\circ \\ \sigma_4 = 2.2^\circ \pm 0.7^\circ \end{cases} \tag{D.17}$$

The inconsistency which is seen with some measurements of σ_Φ could come from offsets adjustments. For a given bar, the raw mean value $<\Delta_{TDC}>=<TDC_{up} - TDC_{down}>$ is not zero. So, an offset is added to all Δ_{TDC} measurements in order to have $<\Delta_{TDC}>=0$. Since $<\Delta_{TDC}>$ was changing during the experiment, different offsets are needed: one has to find offsets for various group of runs (in which $<\Delta_{TDC}>$ seems not to change). But, the error made on the offsets is big when statistics are low. $\mathcal{C}_{-2}$ and $\mathcal{C}_{+2}$ are matrices for the bars which are on the side of the detector, where the cross section is low. Consequently, the error made on the offset determination is bigger than in the other layers of the detector. Such errors artificially increase σ_Φ.

Using bayesian formalism to take into account the uncertainties on $\sigma_{1,2,3,4}$, (D.10) becomes

$$P(D|E_1, \cdots, E_n) \propto e^{-\left(D - \sigma_e^2 \sum_{i=1}^{n} \frac{E_i}{\sigma_i^2}\right)^2 / \, 2\sigma_e^2} \cdot \prod_{i=1}^{4} e^{-\frac{(\sigma_i - \sigma_{0i})^2}{2\sigma^2_{\sigma_{0i}}}} \cdot e^{-\frac{(\sigma_e - \sigma_{0e})^2}{2\sigma^2_{\sigma_{0e}}}} . \quad \text{(D.18)}$$

Integrating (D.18) over $\sigma_{1,2,3,4}$ gives the posterior estimate of D. The standard deviation of the errors are shown in tab D.1 (montecarlo).

Matrix	resolution, from (D.18)	resolution, from (D.6)
$\mathcal{C}_{-2}$	1.2°	1.1°
$\mathcal{C}_{-1}$	1.6°	1.1°
$\mathcal{C}_{0}$	1.3°	1.2°
$\mathcal{C}_{+1}$	1.0°	0.8°
$\mathcal{C}_{+2}$	1.3°	1.1°

Table D.1: Error associated with the different covariance matrices

Bibliography

[1] O. C. Simpson I. Estermann and O. Stern. The Magnetic Moment of the Proton. *Physical Review*, 52:535–545, 1937.

[2] R. W. McAllister R. Hofstadter. Electron Scattering from the Proton. *Physical Review*, 98:217, 1955.

[3] M. R. Yearian and R. Hofstadter. Magnetic form factor of the neutron. *Physical Review*, 110:552–564, 1958.

[4] R. G. Sachs. High-Energy Behavior of Nucleon Electromagnetic Form Factors. *Physical Review*, 126:2256, 1962.

[5] M. N. Rosenbluth. High Energy Elastic Scattering of Electrons on Protons. *Physical Review*, 79:615–619, 1950.

[6] L. Andivahis et al. Measurment of the electric and magnetic form factors of the proton from Q^2=1.75 to 8.83 $(GeV/c)^2$. *Physical Review D*, 50:5491, 1994.

[7] L. E. Price et al. Backward-angle electron-proton elastic scattering and proton electromagnetic form factos. *Physical Review D*, 4:45, 1971.

[8] Günther Kubon. *The neutron magnetic form factor for* $Q^2 < 1(GeV/c)^2$. PhD thesis, Institut für Physik, Universität Basel, 1999.

[9] S. Platchkov et al. Deuteron A(Q^2) structure function and the neutron electric form-factor. *Nuclear Physics A*, 510:740, 1990.

[10] R. Schiavilla and I. Sick. Neutron charge form factor at large q^2. *Physical Review C*, 64:41002, 2001.

[11] N. Dombey. Scattering of Polarized Leptons at High Energy. *Review of modern physics*, 41:236–246, 1969.

[12] R.M. Woloshyn B. Blankleider. Quasi-elastic scattering of polarized electrons on polarized ^3He. *Physical Review C*, 29(2):538–552, 1984.

[13] J. Becker et al. Determination of the neutron electric form factor from the reaction $^3He(e,e'n)$ at medium momentum transfer. *The European Physical Journal A*, 6:329–344, 1999.

[14] D. Rohe et al. Measurement of the neutron electric form factor G_e^n at $0.67(GeV/c)^2$ via $^3\vec{H}e(\vec{e},e'n)$. 83:4257–4260, 1999.

[15] S. Galster et al. Electron Scattering from the Proton. *Nuclear Physics B*, 32:221, 1971.

[16] G. Derrick and J.M. Blatt. Classification of triton wave functions. *Nuclear Physics A*, 8:310–324, 1958.

[17] G. L. Payne et al. Configuration space Faddeev calculations. I. Triton ground state properties. *Physical Review C*, 22:823–831, 1980.

[18] A. Laverne and C. Gignoux. A detailed analysis of ^3H from Faddeev equations in confuguration space. *Nuclear Physics A*, 203:597–608, 1973.

[19] J. L. Friar et al. Neutron polarization in polarized ^3He targets. *Physical Review C*, 42:2310–2314, 1990.

[20] R.-W. Schulze and P. U. Sauer. Inelastic electron scattering from the three-nucleon bound states with polarization. *Physical Review C*, 48:38–63, 1993.

[21] R. C. Walker et al. Measurements of the proton elastic form factors for $1 \leq Q^2 \leq 3$ (GeV/c)^2 at SLAC. *Physical Review D*, 49:5671, 1994.

[22] J. Golak et al. Extraction of electromagnetic neutron form factors through inclusive and exclusive polarized electron scattering on polarized ^3He target. *Physical Review C*, 63:34006, 2001.

[23] W. Glöckle et al. The three-nucleon continuum: achievments, challenges and applications. *Physics Reports*, 274:107, 1996.

[24] J. Golak et al. Electron induced pd and ppn breakup of ^3He with full inclusion of final-state interactions. *Physical Review C*, 51:1638, 1995.

[25] H. E. Conzett. The vanishing analyzing powers in electron-proton elastic scattering; symmetries and dynamics. *Nuclear Physics A*, 628:81–86, 1998.

[26] J. Bermuth et al. The neutron charge form factor and target analyzing powers from $^3\vec{He}(\vec{e},e'n)$-scattering. *Physical Letters B*, 564:199–204, 2003.

[27] Pascal Merle. *Entwicklung des programmierbaren Koinzidenztriggersystems und Messung von* A_Y^0 *in der Reaktion* $^3\overrightarrow{He}(\overrightarrow{e},e'n)$. PhD thesis, 2002.

[28] Jörg Bermuth. *Bestimmung des elektrischen Formfaktors des Neutrons* G_e^n *in der Reaktion bei einem Impulsübertrag* $Q^2{=}0.67(GeV/c)^2$. PhD thesis, Institut für Physik, Johannes Gutenberg-Universität Mainz, July 2001.

[29] K. Aulenbacher et al. The MAMI source of polarized electrons. *Nuclear Instrument and Methods in Physics Research A*, 391:498–506, 1997.

[30] K. I. Blomqvist et al. The three-spectrometer facility at the Mainz microtron MAMI. *Nuclear Instrument and Methods in Physics Research A A*, 403:263–301, 1998.

[31] W. Hartmann et al. A source of polarized electrons based on photoemission of GaAsP. *Nuclear Instrument and Methods in Physics Research A*, 286:1–8, 1990.

[32] H. Herminghaus et al. The Design of a Cascaded 800MeV Normal Conducting C.W. RaceTrackMicrotron. *Nuclear Instrument and Methods in Physics Research A*, 138:1–12, 1976.

[33] F.D. Colegrove et al. Polarization of ^3He Gas by Optical Pumping. *Physical Review*, 132(6):2561–2572, 1963.

[34] G. Eckert et al. A dense polarized ^3He target based on compression of optically pumped gas. *Nuclear Instrument and Methods in Physics Research A*, 320:53–65, 1992.

[35] R. M. Herman. Theory of Spin Exchange between Optically Pumped Rubidium and Foreign Gas Nuclei. *Physical Review A*, 0137(4):1062–1065, February 1965.

[36] E.M Purcell and G.B. Field. Influence of Collisions upon Population of Hyperfine States in Hydrogen. *Astrophysical Journal*, 124:542–549, 1956.

[37] Daniela Rohe. *Messung des elektrischen Formfaktors des Neutrons G_{en} an $^3\vec{He}$ mit dem A1-Elektronspectrometer.* PhD thesis.

[38] W. Heil. Private communication. 2004.

[39] N. R. Newbury et al. Gaseous $^3He -^3 He$ magnetic dipolar spin relaxation. *Physical Review A*, 48:4411–4420, 1993.

[40] R.D. McKeown R.G. Milner and C.E. WoodWard. Study of spin relaxation by a charged particle beam in a polarized ^3He gas target. *Nuclear Instrument and Methods in Physics Research A*, 257:286–290, 1987.

[41] D.P. Saltzberg K.D. Bonnin and W.Happer. Relaxation of gaseous spin-polarized ^3He target due to creation of $^3He^+$. *Physical Review A*, 38(9):4481–4487, 1988.

[42] L. D. Schearer and G. K. Walters. Nuclear Spin-Lattice Relaxation in the Presence of Magnetic-Field Gradients. *Physical Review A*, 39:1398–A1402, 1988.

[43] S.M Harris and R.J. Jabbur. On Depolarization of Fast Positrons by Bremsstrahlung. *Nuovo Cimento*, 32(1):258–260, 1964.

[44] W. Lorenzon et al. NMR calibration of optical measurement of nuclear polarization in ^{3}He. *Physical Review A*, 47:468–479, 1993.

[45] Fabian Parpan. Polarisation von ^3He im Rahmen des Experiments 'Struktur von ^3He'. Master's thesis, Institut für Physik, Universität Basel, 2003.

[46] Richard E.J. Florizone. *The Longitudinal and Transverse Response of the (e,e'p) Reaction in Helium-3 and Helium-4 in the Quasielastic Region.* PhD thesis, Massachusetts Institute of Technology, 1999.

[47] A. Amroun et al. ^3H and ^3He electromagnetic form factors. *Nuclear Physics A*, 579:596–626, 1994.

[48] Manfred Korn. *Entwicklung des Bahnrückverfolgunsverfahrens für die Drei-Spektrometer-Anlage und experimentelle Bestimmung der Abbildungseigenschaften der Spektrometer A und B mit elastischer Elektronenstreuung.* PhD thesis, Institut fr Physik, Johannes Gutenberg-Universität Mainz, 1994.

[49] V.G.J. Stoks R.B Wiringa and R.Schiavilla. Accurate nucleon-nucleon potential with charge-independence breaking. *Physical Review C*, 51:38–51, 1995.

[50] C. Carasco et al. Final State Interaction Effects in $^3\vec{H}e(\vec{e},e'p)$. *Physics Letters B*, 559:41, 2003.

CURRICULUM VITAE

Données personnelles:

Nom:	Cédric Carasco
Date de naissance:	12. Mars 1976
Lieu de naissance:	St-Denis, France (93)
Nationalitée:	Francais
Statut civil:	Célibataire
Addresse:	14, rue du Nord, 68330 Huningue

Education:

1992 - 1994	Lycée Jean Calvin, Compiègne (60), Baccalaureat série C, mention assez bien.
1994 - 1996	Lycée Pierre d'Ailly, Compiègne (60), Mathematiques supérieures et Spéciales M.
1996 - 1999	Ecole Nationale Supérieure d'Ingénieurs de Caen, Institut des Sciences de la Matière et du Rayonnement (ISMRa). Diplome d'ingénieur en Instrumentation Nucléaire. Diplome d'Etudes Approfondies «Mesure Capteur Image».

Activitées scientifique:

1998	Commissariat à l'Energie Atomique (CEA), centre de Saclay. Stage au Service d'Etude des Detecteurs (SED), sous la direction de Philippe Rebourgeard, sur les claquages des chambres MICROMEGAS.
Depuis 1999	Assistant au 4MV Praktikum de l'Université de Bales, Participation aux experiences du groupe du Professeur Sick a MAMI (Mayence), PSI (Villigen) et JLab (Newport News).

Publications:

D. Thers et al., Micromegas as a large microstrip detector for the COMPASS experiment, *Nuclear Instruments and Methods in Physics Research A* 469, 133 (2001)

Ph. Abbon et al. Micromegas, a microstrip detector for Compass, *Nuclear Instruments and Methods in Physics Research A* 461 , 29 (2001)

C. Carasco et al. Final State Interaction Effects in $^3\vec{H}e(\vec{e},e'p)$, *Physical Letters B* 559, 41 (2003)

G. Kubon et al. Precise Neutron Magnetic Form Factor, *Physical Letters B* 524, 26 (2002)

J. Bermuth et al. The neutron charge form factor and target analyzing powers from $^3\vec{H}e(\vec{e},e'n)$-scattering *Physical Letters B* 564, 199 (2003)

G. Warren et al. Measurement of the Electric Form Factor of the Neutron at $Q^2 = 0.5$ and 1.0 $(\mathrm{GeV/c})^2$ *Physical Review Letters* 92, 42301 (2004)